Article:
Wang, Z, Peacock, C orcid.org/0000-0003-3754-9294, Kwon, KD et al. (3 more authors) (2023) Site-specific isotope fractionation during Zn adsorption onto birnessite: Insights from X-ray absorption spectroscopy, density functional theory and surface complexation modeling. Geochimica et Cosmochimica Acta, 348. pp. 68-84. ISSN 0016-7037

https://doi.org/10.1016/j.gca.2023.03.006

Prepared for *Geochim. Cosmochim. Acta*

Site-specific isotope fractionation during Zn adsorption onto birnessite: Insights from X-ray absorption spectroscopy, density functional theory and surface complexation modeling

Zhao Wang[a,b,f], Caroline Peacock[b], Kideok D. Kwon[c], Xueyuan Gu[d], Xionghan Feng[e], Wei Li[a,f*]

[a] Key Laboratory of Surficial Geochemistry, Ministry of Education, School of Earth Sciences and Engineering, Nanjing University, Nanjing 210023, China

[b] School of Earth and Environment, University of Leeds, Leeds, LS2 9JT, UK

[c] Department of Geology, Kangwon National University, Chuncheon 24347, Republic of Korea

[d] State Key Laboratory of Pollution Control and Resources, School of Environment, Nanjing University, Nanjing, 210023, China

[e] State Environmental Protection Key Laboratory of Soil Health and Green Remediation, College of Resources and Environment, Huazhong Agricultural University, Wuhan 430070, China

[f] Frontiers Science Center for Critical Earth Material Cycling (FSC-CEMaC), Nanjing University, Nanjing, Jiangsu, 210023, China

* Corresponding author, Email: liwei_isg@nju.edu.cn

Abstract

Birnessite minerals help control the fate of Zn in surface environments and readily fractionate Zn isotopes through adsorption reactions, yet little is known about the role played by various reactive sites in stable isotopic fractionation. Here we present the Zn isotope fractionation data cause by adsorption on birnessite under different reaction times, pH values, and Zn concentrations. We observe that isotopic equilibrium of Zn is attained after ~120 h of reaction time at pH 6. At pH 3−5 and Zn concentrations of 0.05−0.3 mM, the isotopic fractionation ($\Delta^{66}Zn_{adsorbed\text{-}aqueous}$) is around -0.46 ± 0.04‰, and gradually increases to -0.09 ± 0.05‰ at pH 6−8 and Zn concentrations of 0.2 mM. The change in Zn isotopic compositions as a function of pH and Zn concentration is well described using the surface complexation model, where two binding sites are involved: external edge sites and interlayer vacancies. According to this model, two different isotopic fractionation factors of Zn are calculated: $\Delta^{66}Zn_{adsorbed\text{-}aqueous}$ = -0.46 ± 0.04‰ for adsorption on vacancy sites and $\Delta^{66}Zn_{adsorbed\text{-}aqueous}$ = 0.52 ± 0.04‰ for binding to edge sites. Extended X-ray absorption fine structure spectroscopy (EXAFS) demonstrates that Zn forms triple-corner-sharing (TCS) octahedral complex on birnessite vacancies at pH 3 and Zn concentrations of 0.05−0.2 mM, where Zn is coordinated on one side to three oxygen atoms of the Mn vacancy (~2.03 Å) and to three water molecules on the other side (~2.15 Å), suggesting the formation of distorted Zn−O octahedra (average bond length: ~2.09 Å). At pH 6 and 8, double-corner-sharing (DCS) complexes on layer edges formed in addition to the TCS

41 octahedral complex on vacancies. Density functional theory (DFT) optimisations suggest
42 that DCS Zn complex exist in tetrahedral coordination. Based on EXAFS spectroscopy,
43 DFT optimisations and surface complexation modeling, the distinct isotopic fractionation
44 of Zn is related to the differences in Zn local structure at different reactive sites of birnessite.
45 Our results provide a molecular-scale understanding of Zn isotopic fractionation in natural
46 birnessite-containing settings, as well as new insights into predicting the links between
47 adsorption and fractionation of other similar metals.

48

49 *Keywords: Birnessite; adsorption; isotope fractionation; SCM; EXAFS; DFT*

1. Introduction

Birnessite is a nanosized variety of poorly crystalline phyllomanganate that occurs widely in freshwater (Manceau et al., 2007), soils (Hochella et al., 2005), and marine sediments (Peacock and Sherman, 2007a). The crystal structure of birnessite is composed of layered edge-sharing MnO_6 octahedra, and the distance between layers is approximately 7.2 Å (Manceau et al., 2002). Due to the presence of Mn vacancies and lower valence cations substitution for Mn^{4+} in the MnO_6 layers (Lanson et al., 2002; Toner et al., 2006; Peacock, 2009; Kwon et al., 2009), the surface of birnessite is negatively charged, which leads to the adsorption of multivalent cations. For example, Zn^{2+}, Ni^{2+}, or Cu^{2+} adsorbs as triple-corner-sharing (TCS) surface complex (Fig. 1a-b) (Manceau et al., 2002; Peacock, 2009; Kwon et al., 2009), or Cu^{2+} and Ni^{2+} incorporate into Mn vacancy sites (INCs) as part of the birnessite layer (Fig. 1c) (Peacock and Sherman, 2007b). In addition, at birnessite particle edges, the undercoordinated oxygen atoms can adsorb cations by forming double-corner-sharing (DCS) or double-edge-sharing (DES) complexes (e.g., Ni^{2+}, Co^{2+}, or Pb^{2+}) (Fig. 1d-f) (Villalobos et al., 2005; Bargar et al., 2009; Kwon et al., 2010; Simanova et al., 2015; Wang et al., 2018).

As a result of its common occurrence and high surface reactivity, birnessite plays a fundamental role in trace metal cycling, exerting a strong control on the fate and mobility of trace metals through sorption reactions (Post, 1999; Sherman and Peacock, 2010). In the ocean, for example, trace elements (e.g., Zn, Cu, and Ni) are enriched in poorly crystalline

birnessite in ferromanganese crusts by 10^6 times over their concentrations in seawater (e.g., Koschinsky and Hein, 2003). Birnessite has also been reported to influence the cycling of trace metals in terrestrial environments (Manceau et al., 2007) and in areas influenced by anthropogenic activities from mining and smelting activities (Juillot et al., 2011; Spinks and Uvarova, 2019).

The environmental biogeochemical cycling of metals can be investigated by applying of metal stable isotope systems, since the metal isotopic signatures can be used to identify the specific sources and geochemical processes (e.g., Chen et al., 2008; Wiederhold, 2015). Metal stable isotopes, for example, have been shown to have the potential to distinguish between anthropogenic and natural sources of metals and thus enable fingerprinting of environmental pollution (Aranda et al., 2012; Bi et al., 2017). The isotopic signatures from different sources can be obscured, however, by isotopic fractionation during mineral-solution interface reactions (e.g., Gueguen et al., 2018; Wang et al., 2022), which may hamper the application of metal isotopes as effective tracers.

Similarly, metal stable isotopes have also been used to quantify the input and output of metal marine budgets (Gall et al., 2013; Little et al., 2014b). Marine sediment adsorption controls the output of trace metals from the ocean; however, this process can drive significant isotopic fractionation but is poorly constrained (Vance et al., 2016; Liu et al., 2019; Sorensen et al., 2020). In general, investigating the links between isotopic fractionation and adsorption can improve the understanding of fractionation and inform the

most accurate use of metal isotopes in environmental investigations.

Zinc (Zn) and its isotopes are ideal candidates to examine the links between adsorption and fractionation because we already know some information about Zn adsorption and fractionation with Mn oxides (e.g., Pokrovsky et al., 2005; Bryan et al., 2015). Previous work on the isotopic fractionation and the coordination environment of Zn during adsorption to different mineral surfaces can inform experimental design and interpretation (e.g., Pokrovsky et al., 2005). Pokrovsky et al. (2005) firstly reported the isotopic fractionation values of Zn caused by adsorption on various metal oxides, suggesting that adsorption of Zn onto surfaces of hematite, pyrolusite, corundum and gibbsite enriches heavier Zn isotopes, while birnessite and goethite prefer to adsorb lighter Zn isotopes. Later, Bryan et al. (2015) found that Zn isotopes show complicated behaviour during adsorption to birnessite, which may be affected by both Zn surface coverage and solution ionic strength. At low ionic strength, insignificant Zn isotope fractionation ($\Delta^{66}Zn_{adsorbed–aqueous}$ = 0.05 ± 0.08‰) is observed. In high ionic strength solution, heavy Zn are enriched on the birnessite surface, but the isotopic fractionation is strongly dependent on surface coverage, with $\Delta^{66}Zn_{adsorbed–aqueous}$ = 0.16‰ at high surface coverage, which is increased to 2.74‰ at low surface coverage. Additionally Zn is a micronutrient required by organisms and is also a potential contaminant in many scenarios (e.g., Moore et al., 2013; Sandstead, 2014). For example, Zn plays a key role as a cofactor in carbonic anhydrase involved in carbon fixation, so their concentrations in seawater are critical for regulating climate (Morel et al.,

1994). In the ocean the concentration and isotopic compositions of Zn is controlled by adsorption to ferromanganese (oxyhydr)oxides in ferromanganese crusts and nodules and in ferromanganese particulates in oxic sediments (Little et al., 2014)

Knowledge of Zn surface coordination chemistry is key to understand the complex behaviour of Zn isotopes during interfacial adsorption reactions. Classic stable isotope exchange theory (Bigeleisen and Mayer, 1947) suggests that equilibrium isotopic fractionation is controlled by the bond strength between the metal of interest and its neighboring atoms (Schauble, 2004). As an advanced technique based on synchrotron radiation accelerator, EXAFS spectroscopy can determine the bond distance and coordination number of metals adsorbed on mineral surfaces. This molecular-level information can be related to isotopic behaviour to elucidate the relation between interfacial reactions and isotopic fractionation (e.g., Juillot et al., 2008). At present, Zn isotopic fractionation mechanisms have been examined for several different mineral systems by EXAFS spectroscopy (e.g., Nelson et al., 2017; Wang et al., 2022). In the Zn-γ-Al_2O_3 system, adsorption of heavy Zn ($\Delta^{66}Zn_{adsorbed-aqueous}$ = 0.47 ± 0.03‰) is explained by the presence of tetrahedral Zn with a typically shorter Zn-O bond length (1.96 Å) relative to aqueous Zn (2.06 Å) (Gou et al., 2018). Similarly, in iron oxide systems, the enrichment of heavier Zn isotopes on solid phases is related to a shorter Zn-O bond length of adsorbed Zn relative to the aqueous phase (Juillot et al., 2008). Recently, Wang et al. (2022) observed insignificant isotopic fractionation owing to the formation of outer-sphere octahedral Zn

complexes on todorokite, in which there is no obvious change in the coordination environment relative to aqueous Zn. Despite different coordination numbers, the formation of octahedral and tetrahedral Zn complexes results in undistinguishable isotopic fractionation factors in silica systems (Nelson et al., 2017). This lack of isotopic fractionation is proposed to be caused by the small energy difference between octahedral and tetrahedral Zn species on amorphous silica and quartz surfaces (Nelson et al., 2017). For Zn adsorption on birnessite, Zn isotopes are shown to have complicated behaviour influenced by surface coverage and solution ionic strength, and different studies produce disparate results (Pokrovsky et al., 2005; Bryan et al., 2015). To date, EXAFS has not been applied to explain this complicated isotopic behaviour.

In this study, we investigate the adsorption of Zn onto birnessite and examine the associated isotopic fractionation behaviour under different contact times, pH values, and Zn concentrations. We follow a synergetic EXAFS spectroscopy, DFT geometry optimisation, and surface complexation modeling (SCM) approach to elucidate the fractionation mechanisms of Zn isotopes. The molecular-level structural information revealed by EXAFS spectroscopy and DFT optimisation sheds light on the nature of surface complex of Zn on birnessite and allows interpretation of the equilibrium isotopic fractionation. Additionally, we use the adsorption complexes provided by EXAFS and DFT to constrain the SCM modeling. SCM allows us to quantitatively constrain the site-specific fractionation factors of Zn isotopes caused by adsorption on birnessite. These results offer

a mechanistic understanding of the site-specific fractionation behaviour of Zn and potentially new insights into the links between adsorption and fractionation of other similar metals.

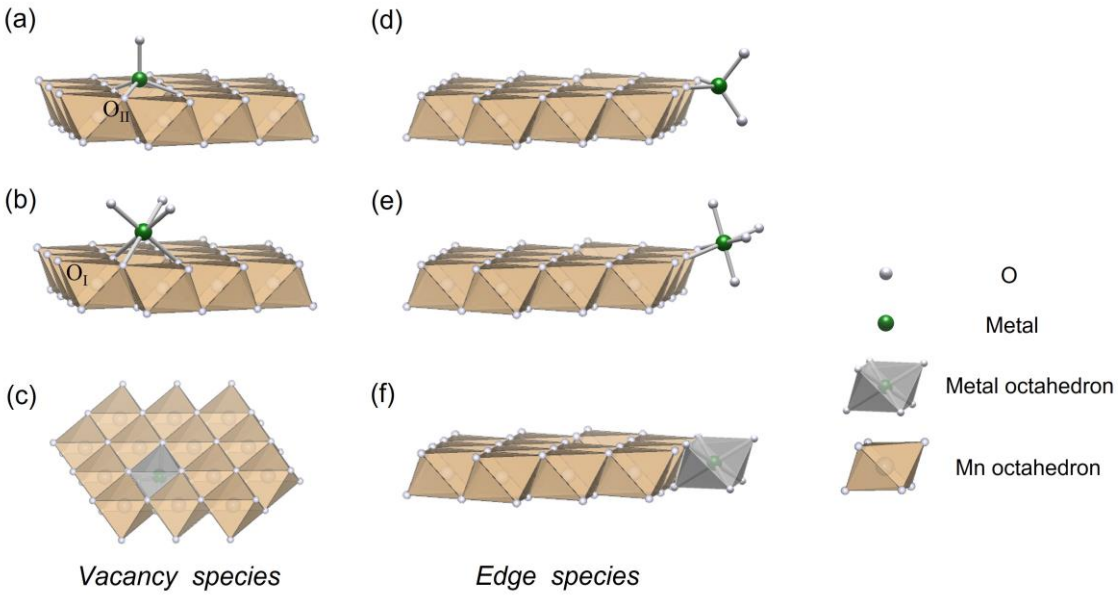

Fig. 1 Schematic representations of possible surface complexes of metals on birnessite: (a) metal-TCS complex in tetrahedral coordination and (b) metal-TCS complex in octahedral coordination associated with vacancy sites; (c) incorporation of a metal cation into a birnessite layer vacancy; (d) metal-DCS complex in tetrahedral coordination and (e) metal-DCS complex in octahedral coordination associated with edge sites; (f) metal-DES complex in octahedral coordination associated with edge sites. O_I and O_{II} depict singly coordinated and doubly coordinated oxygen atoms, respectively. Yellow octahedra: Mn; white spheres: O; gray octahedra and green spheres: metals.

2. Materials and Methods

2.1. Synthesis of birnessite

Acid birnessite was synthesised following the procedure described by McKenzie (1971). First, 500 mL of 0.4 mol/L $KMnO_4$ solution was heated to boil in an oil bath. Then,

168 a 35 mL mixed solution of 12 mol/L HCl and 15 mL doubly deionized water (18.2 MΩ,
169 Milli-Q, Millipore) was added slowly to the $KMnO_4$ solution at a speed of 0.7 L/min. After
170 30 min, the crystal suspension was cooled at ambient temperature and then aged for ~12 h
171 at ~60 °C (Feng et al., 2007). The resulting precipitates were separated by centrifugation
172 and rinsed with deionized water until Cl^- cannot be detected by 0.1 mol/L acidic $AgNO_3$
173 solution and then freeze-dried. The background Zn concentration in the synthetic birnessite
174 was determined to be very low (i.e., 4.2 ppm). This low Zn concentration in the birnessite
175 has a negligible impact in our adsorption experiments and isotopic measurements.
176
177 **2.2. Characterisation of birnessite**
178 A Bruker D8 diffractometer (Mo Kα radiation) was employed to collect the powder
179 X-ray diffraction (XRD) patterns of the birnessite with an operation voltage of 40 kV/30
180 mA. Samples were analyzed over a 5°-80° 2θ angular range with a step size of 0.02° and 1
181 s counting time per step.
182 Transmission electron microscopy (TEM) images of the synthetic birnessite were
183 collected on an FEI Tecnai (F20) microscope at an accelerating voltage of ~200 kV. For
184 imaging, finely ground sample powders were suspended and dispersed in ethanol using a
185 sonication bath. Holey carbon grids were used to load samples. The specific surface area
186 of the birnessite was measured by the N_2 Brunauer-Emmet-Teller (BET) method to be 30.7
187 $m^2\ g^{-1}$. Using an oxalic acid/permanganate back-titration method (Feng et al., 2007), the

188 average oxidation state (AOS) of Mn in our synthetic birnessite was measured to be 3.92.

189

190 **2.3. Zinc adsorption experiments**

191 Three different types of adsorption experiments were conducted: 1) kinetic adsorption
192 experiments at pH ~ 6 and Zn concentration of ~0.2 mM for a duration of 0.5 − 432 h; 2)
193 adsorption edge experiments at Zn concentration of ~0.2 mM in different ionic strength
194 solutions (I = 0.01 and 0.1 M $NaNO_3$) at pH 3−9 for 120 h; and 3) adsorption isotherm
195 experiments (I = 0.1 M $NaNO_3$) at pH ~3 and pH ~7 with Zn concentrations of 0.05−0.3
196 mM for 120 h.

197 Prior to Zn addition, ~0.065 g L^{-1} birnessite suspension was equilibrated at a fixed pH
198 between 3 and 9 for ~24 h in I = 0.1 M $NaNO_3$ solutions (except for adsorption edge
199 experiments in I = 0.1 M and 0.01 M $NaNO_3$ solutions). After this hydration step, certain
200 amounts of ~35 mM $Zn(NO_3)_2$ stock solution were added to the birnessite suspension,
201 resulting in the desired Zn concentrations of 0.05−0.3 mM. These initial Zn concentrations
202 were selected because the concentrations of Zn adsorbed on birnessite (0.037 < Zn/Mn
203 molar ratio < 0.327) not only covered previously investigated Zn range, but also
204 complemented the higher Zn part, which is essential to elucidate the link between Zn
205 adsorption and fractionation on birnessite and further apply to natural systems with
206 different Zn concentration. The Zn stock solution was added dropwise over a period of
207 several minutes, while the suspensions were stirred vigorously to ensure no local

208 oversaturation of any Zn solid phases (e.g., Zn hydroxides and hydrozincite) present in the
209 solution. Thermodynamic calculations from Visual MINTEQ.3.1 suggest that the
210 predominant Zn species was free $Zn(H_2O)_6^{2+}$ across the pH range 3–8 in the adsorption
211 experiments (Fig. S1).

212 After the reaction (detailed in Table 1), the suspension was centrifuged to separate the
213 solid and solution phases. The solution was then filtered using ~0.22 μm polyethersulfone
214 membrane filters (Sartorius, Germany). The Zn concentration was analysed using an
215 inductively coupled plasma-optical emission spectrometer (ICP−OES) (iCAP 6000,
216 Thermo). Selected fresh paste solids were collected for EXAFS analysis. Procedural blank
217 experiments were included in each set of adsorption experiments (kinetic, adsorption edge,
218 and isotherm experiments) to monitor the potential Zn contamination. All experiments used
219 reagent grade chemicals, doubly deionized water, and purified acids (via double sub-
220 boiling distillation). Teflon labware was used to minimize potential Zn contamination for
221 both adsorption and isotopic experiments.

222

223 **2.4. Zinc isotope measurements**

224 After batch adsorption experiments, the supernatants obtained were dried and then
225 dissolved in ~11 M HCl prior to Zn isotope analysis. The birnessite samples (after
226 adsorption and centrifugation) were completely digested in ~11 M HCl to dissolve the
227 birnessite and release adsorbed Zn. Then the solution was evaporated to dryness and

redissolved in approximately 2 M HCl, and the solution was loaded in Teflon columns (height: 10 cm, diameter: 0.4 cm) containing AG MP-1 (100–200 mesh) anion-exchange resin (Bio−Rad, USA). Zn was purified following the same protocol by Wang et al. (2022). For each experimental run, the procedural blanks of Zn (< 20 ng) were negligible, because ~25 μg Zn was used for isotopic determination of each sample. After purification, the sample was evaporated to dryness and redissolved in ~15 M HNO_3 to eliminate organic resin residues. The solution was then evaporated to dryness again before the sample was dissolved in ~0.05 M HNO_3 for Zn isotope analysis.

Zn isotopic compositions were measured using a Neptune Plus multicollector inductively coupled plasma mass spectrometer (MC−ICP−MS) (Thermo Scientific). Both empirical external normalization (EEN) (i.e., doping with ERM-AE647 Cu) and the sample standard bracketing (SSB) methods were used for mass bias correction (Marechal et al., 1999). Standard and sample solutions were diluted to ~0.2 ppm Cu and ~0.5 ppm Zn for measurements. The Zn isotope analysis for each sample was performed for three blocks of 60 cycles. The introduction system was washed for 40 s before each isotopic ratio measurement using a 0.05 M HNO_3 solution to bring the Zn signal to the baseline value. The take-up time was ~180 s for each measurement. The isobaric interference of ^{64}Ni on ^{64}Zn was evaluated by collecting ^{62}Ni, but the impact was found to be negligible. The measurements were run using wet plasma at low mass resolution modes.

The measured Zn isotope composition was provided in delta notation for $^{66}Zn/^{64}Zn$

relative to our in-house standard (HPS) (Wang et al., 2022) as follows:

$$\delta^{66}Zn = (((^{66}Zn/^{64}Zn)_{sample}/(^{66}Zn/^{64}Zn)_{HPS}) - 1) \times 1000\ (‰) \quad (1)$$

We used the IRMM 3702 and JMC Lyon international standards to calibrate our in-house standard which gave $\delta^{66}Zn_{HPS}$= -0.36±0.04‰ and -0.07±0.04‰, respectively (Wang et al., 2022). Over a 4-year period, the MC-ICP–MS achieved a long−term external reproducibility better than 0.03‰ (2SD) for $\delta^{66}Zn$ based on a record of repeated analyses of geological rock standards and synthetic solutions. Several geological rock standards, such as Nod-P-1 and BCR, were analysed to assess the accuracy of the analytical procedure, which is comparable to previously reported values within error (Wang et al., 2022).

Zn isotopic fractionation ($\Delta^{66}Zn_{adsorbed\text{-}aqueous}$) between the adsorbed and aqueous phases and the mass balance offset (O) were calculated using the following two equations:

$$\Delta^{66}Zn_{adsorbed\text{-}aqueous} = \delta^{66}Zn_{adsorbed} - \delta^{66}Zn_{aqueous} \quad (2)$$

$$O = \delta^{66}Zn_{stock} - (\delta^{66}Zn_{adsorbed} \times f + \delta^{66}Zn_{aqueous}(1 - f)) \quad (3)$$

where O and f are the mass balance offset and the percent of Zn adsorption, respectively. The mass balance values are considered acceptable, if they are within the 0.06‰ uncertainty (2SD) of the initial Zn stock ($\delta^{66}Zn_{stock}$ = 0.28 ± 0.06 ‰).

2.5. EXAFS data collection and analysis

The Zn *K*-edge EXAFS data were collected at Beijing Synchrotron Radiation Facility (BSRF) and Shanghai Synchrotron Radiation Facility (SSRF) on 1W1B beamline and

14W1B beamline, respectively. For both beamlines, the beamline monochromator consists of two parallel Si(111) crystals. Higher-order harmonics were rejected by detuning the two parallel Si(111) crystals by 30%. Experimental spectra were recorded by scanning energy from about 9570 eV to10200 eV. Energy steps were of 10 eV for the pre-edge range, 1ev for the absorption edge, 0.05Å for the post-edge range and counting time for each point varied from 2 s to 5s depending on the signal sensitivity. Calibration of the energy was performed against a Zn foil (~9659 eV). Solid samples were prepared as fresh pastes from adsorption experiments, and were mounted into plastic holders in both sides sealed using Kapton tape to prevent from sample dehydration. Samples with high Zn loading (e.g., >2% by weight) were analysed in transmission mode and otherwise in florescence mode. Three to five scans were collected for each sample to achieve a good signal/noise ratio. In addition to the adsorption samples, a series of Zn reference samples were also examined including Zn hydroxide, hydrozincite, chalcophanite, and tetrahedral Zn on birnessite (Table 2).

The IFEFFIT 1.2.11 program was used to process the EXAFS data. The $\chi(k)$ function was extracted and weighted by k^3 to enhance the oscillation in higher k range. In Fourier transform, k range of 3-11 $Å^{-1}$ and the Hanning window function was used. For all samples, shell-by-shell fitting was performed in R-space in the range of 1.0-3.6 $Å^{-1}$. The Zn-O, Zn-Zn and Zn-Mn paths were calculated using a chalcophanite structural model. Fitting of the spectrum of $Zn(NO_3)_2$ solution returned an amplitude reduction factor (S_0^2) of ~0.97 (Wang et al., 2022) and this value was then applied to other samples. In each sample, the single

288 energy shift ΔE_0 was set to be equivalent for all shells.

289

290 **2.6. DFT geometry optimization**

291 Model Zn surface complexes were constructed based on an edge-sharing Mn
292 octahedral nanodisk with a diameter of approximately 1.5 nm (i.e., $Mn_{19}O_{54}H_{30}$). For TCS
293 species, a Mn(IV) vacancy was created by removing one Mn ion, and two Zn ions were
294 placed above and below the vacancy site. Each Zn was coordinated with one or three H_2O
295 molecules to represent a tetrahedral or octahedral coordination, respectively. DCS Zn was
296 initially coordinated to two singly coordinated O atoms at the lateral edge of the vacancy-
297 free nanodisk, and four or two H_2O molecules were added to the Zn cation to represent an
298 octahedral or tetrahedral complex. For the DES Zn complex, $Zn{\cdot}3H_2O$ was coordinated
299 either to one triply coordinated O or one doubly coordinated O of the vacancy-free
300 nanodisk as well as two singly coordinated O at the lateral edge. Each Zn complex model
301 placed in a large periodic cell of 40 × 40 × 30 Å was geometry-optimized using CASTEP
302 code with the spin-polarized generalized gradient approximation using Perdew-Burke-
303 Ernzerhof functional and ultrasoft pseudopotentials (Vanderbilt, 1990; Perdew et al., 1996).
304 The expansion of the plane wave basis set was truncated at 500 eV, and the *k*-point grid
305 was 1 × 1 × 1 for the first Brillouin zone. See previous studies (Kwon and Sposito, 2015;
306 Simanova et al., 2015) for the convergence of calculated structural parameters in terms of
307 the supercell size and the kinetic energy cutoff. Geometry optimization was performed with

all atomic positions relaxed using the Broyden, Fletcher, Goldfarb, Shanno (BFGS) procedure (Pfrommer et al., 1997) until the total energy change was less than 5×10^{-6} eV/atom, and the force and atom displacement along any Cartesian component were less than 0.01 eV/Å and 0.0005 Å, respectively. The magnetic ordering among Mn ions was set to be ferromagnetic for simplicity. For some complex models, we used the dispersion correction method (DFT–D) of Grimme (2006).

2.7. Surface complexation modeling

Layered birnessite has both internal surfaces and external surfaces (e.g., Peacock and Sherman, 2007b). For the internal surfaces of birnessite, doubly coordinated oxygens (O_{II}) were associated with vacancy sites (Fig. 1a). For birnessite external surfaces, there were both singly coordinated and doubly coordinated oxygen atoms (Fig. 1b). Both doubly coordinated ($\equiv Mn_2O^{-2/3}$) and singly coordinated oxygens ($\equiv MnOH^{-1/3}$) showed incomplete oxygen coordination, and the resulting negative oxygen charges yielded a natural tendency toward cation binding (Peacock and Sherman, 2007b; Li et al., 2020). The triply coordinated oxygens ($\equiv Mn_3O^0$) on the internal surfaces were considered inert because of the completely satisfied oxygen valence.

A two-site model was used to describe the birnessite surface by including both doubly coordinated interlayer sites, $\equiv Mn_2O^{-2/3}$, and singly coordinated edge sites $\equiv MnOH^{-1/3}$ in this model (Zhao et al., 2018). A constant capacity model (CCM) was chosen to describe

328 the electrostatic effects of the internal surfaces because the interlayer space between two
329 opposing MnO_6 surfaces is too small for a detailed electrical double layer model (Appelo
330 and Postma, 1999). The CCM model was based on the following two assumptions: 1)
331 mineral surfaces only hold one adsorption electrostatic plane, and 2) all surface species
332 were exclusively inner-sphere complexes. The capacitance for the internal sites in the CCM
333 model was optimised based on the adsorption data.

334 For the external surfaces, charge−distribution multisite ion complexation
335 (CD−MUSIC) combined with the triple-layer model (TLM) was used (Komárek et al.,
336 2015; Zhao et al., 2018; Li et al., 2020). Two adsorption electrostatic planes (0−, 1−plane)
337 and one diffusion plane (2−plane) are included in the TLM model. The capacitances of the
338 inner and outer layers in the TLM model were set equal ($C_1 = C_2$) based on previous
339 experimental observations (Sverjensky, 2005). It was supposed that charges of Zn surface
340 complexes distributed between the 1−plane and the 0−plane.

341 ECOSAT 4.9 and the associated fitting program FIT (Keizer and van Riemsdijk, 2009)
342 were used to model the adsorption reactions on the basis of the speciation data obtained
343 from EXAFS and DFT (which showed that the two most likely Zn species associated with
344 birnessite vacancy and edge sites were TCS and DCS configurations, respectively). Zn
345 affinity constants were calculated from the fitting of Zn adsorption data. The model
346 parameters were finally optimized to yield the best linear correlation between the modeled
347 and measured Zn concentrations (Fig. S2, $R^2 = 0.90$ and $p < 0.00001$).

3. Results

3.1 Characterization of synthetic birnessite

Synthetic birnessite (Fig. 2a) shows four broad XRD peaks at ~7.2 Å (001), ~3.6 Å (002), ~2.4 Å (100), and ~1.4 Å (110), which match well with those of typical birnessite (JCPDS 23–1239). The TEM image (Fig. 2b) shows that the particles of synthetic birnessite consist of clusters or spheroidal aggregates with a size of approximately 200 nm, in accordance with the morphology of balls of needles shown in previous studies (e.g., Atkins et al., 2014). The measured interlayer thickness of the birnessite is ~5.7 Å (Fig. 2c), which is less than the 7.2 Å *d*-spacing determined via XRD, indicative of the loss of interlayer water that can occur under the high vacuum conditions required for TEM measurement (Atkins et al., 2014). The characteristic diffraction peaks together with spheroidal morphologies confirm that birnessite was successfully synthesized.

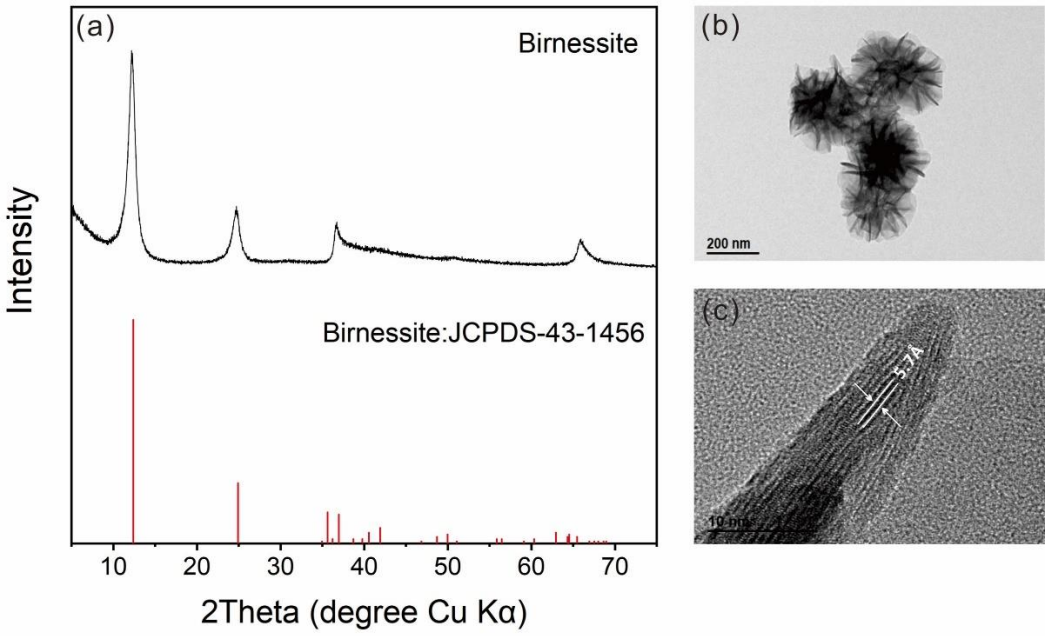

361

362

363 **Fig. 2.** XRD patterns (a) and TEM images (b, c) of synthetic birnessite. PDF JCPDS-43-
364 1456 for birnessite is shown for visual comparison.

365

366 **3.2 Batch adsorption experiments**

367 The result of the kinetic experiment on Zn adsorption to birnessite is presented in Fig.
368 3a. Within the first 24 h, a relatively fast reaction occurs, accounting for ~35% of the total
369 adsorbed Zn. Following the fast adsorption stage, the reaction continues for ~120 h (~42%
370 of the total Zn). At longer reaction times, only a small amount of additional adsorption
371 occurs. After 432 h, ~49% of the initially added Zn is adsorbed. 120 h of reaction time is
372 selected for subsequent experiments.

373 The effects of pH and ionic strength on Zn adsorption on birnessite are shown in Fig.
374 3b. Typically, an increase in the Zn adsorption percentage from ~36% to ~96% occurs with

increasing pH from 3–9. Zinc adsorption did not significantly vary at ionic strength of either 0.01 or 0.1 M, suggesting the formation of an inner-sphere surface complex since metal adsorption via this mechanism can occur regardless of background electrolyte competition (Roberts et al., 2003).

Isotherm experiments of Zn on birnessite at pH 3 and 7 at ionic strengthen of 0.1 M are shown in Fig. 3c. At pH 3, Zn adsorption slowly increases with Zn solution concentration and reaches a plateau (~1.0 mmol g^{-1}) at high Zn concentrations. In contrast, at pH 7, Zn adsorption shows a sharp increase with increasing Zn concentration in solution, resulting in a large Zn adsorption that is more than 2.5 times higher than that at pH 3. Mechanisms for the rapid increase of Zn adsorption at pH 7 is further discussed using the surface complexation modeling described in the following section.

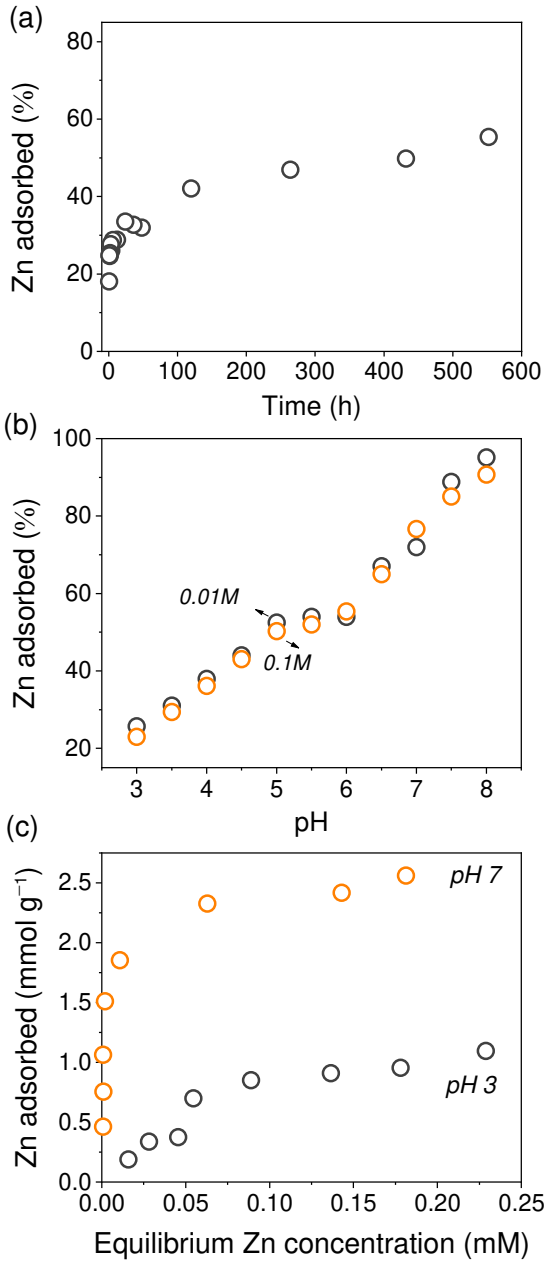

Fig. 3. (a) Kinetics of Zn adsorption onto birnessite at pH 6; (b) Zn adsorption as a function of pH and ionic strength (0.01/0.1 M $NaNO_3$); (c) Adsorption isotherm of Zn at pH 3 and 7 in 0.1 M $NaNO_3$ solution. The Zn concentration was set to 0.2 mM except for the isotherm experiments. The birnessite suspension was 0.065 g/L, and the experimental temperature was 25 ± 1 °C.

3.3 Isotopic fractionation of Zn caused by adsorption

Fig. 4a shows the changes in Zn isotopic compositions ($\delta^{66}Zn$) of the aqueous and adsorbed Zn as a function of time (Table 1). Compared to the $\delta^{66}Zn$ value of the initial Zn solution (i.e., +0.28 ± 0.06‰, 2 SD, n = 6), lighter Zn isotopes are preferentially adsorbed onto the birnessite surface, resulting in heavier isotopes enriched in the aqueous phase. During the first ~120 h of reaction, the $\delta^{66}Zn$ value of the adsorbed phase increases rapidly from -0.61‰ to 0.08‰. Simultaneously, the $\delta^{66}Zn$ value of aqueous Zn decreases from 0.62‰ to 0.44‰. As the adsorption experiment continues from ~120 h to ~432 h, the $\delta^{66}Zn$ values of the adsorbed (0.14 ± 0.08‰) and aqueous phases (0.44 ± 0.05‰) remain almost constant. The corresponding isotopic fractionation value ($\Delta^{66}Zn_{adsorbed\text{-}aqueous}$) changes from -1.23‰ to -0.36‰ during the first ~120 h and then remains nearly unchanged as the experiment proceeds (Fig. 4b and Table 2). This result indicates that fractionation equilibrium is achieved after approximately 120 h of adsorption.

The pH–dependent changes in the isotopic compositions of Zn are shown in Fig. 5 and Table 1. The $\delta^{66}Zn$ value of the adsorbed phase increases gradually from -0.06‰ to 0.28‰ over a pH range of 3 to 9. The $\delta^{66}Zn$ value of the aqueous phase remains nearly unchanged at approximately 0.45‰ at pH 3 to 6 before it decreases to ~0.35‰ and then remains almost unchanged when the pH value of the starting solution increases from 7 to 9. The corresponding $\Delta^{66}Zn_{adsorbed\text{-}aqueous}$ remains almost the same, with an average value

of –0.44 ± 0.05‰ in the pH 3 to 5 range, while the $\Delta^{66/64}Zn_{adsorbed\text{-}aqueous}$ value increases from –0.25 ± 0.06‰ to –0.09 ± 0.06‰ in the pH 6 to 9 range (Fig. 5b).

The adsorption isotherm experiment was conducted to investigate the Zn isotopic fractionation behavior during adsorption at pH 3 (Fig. 5 and Table 1). Continuous enrichment of light Zn isotopes on the birnessite surface relative to aqueous solution is observed (Fig. 5c). As the initial Zn concentration increases, the $\delta^{66}Zn$ value of the adsorbed phase changes from 0.05‰ at $[Zn]_{initial}$ = 0.05 mM to -0.13‰ at $[Zn]_{initial}$ = 0.3 mM. Aqueous compositions decrease correspondingly from 0.46‰ at $[Zn]_{initial}$ = 0.05 mM to 0.37‰ at $[Zn]_{initial}$ = 0.3 mM. The corresponding $\Delta^{66}Zn_{adsorbed\text{-}aqueous}$ remains nearly constant at –0.45 ± 0.06‰ (Fig. 5d). The mass balance offset is within ± 0.05‰ of the isotopic composition of the starting solution (Table 1), suggesting the robustness of the isotopic data.

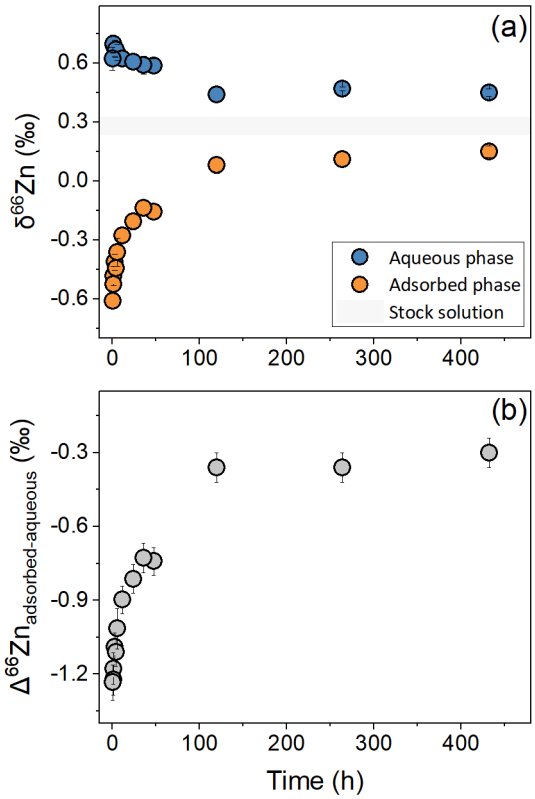

Fig. 4. Changes in the isotopic composition of Zn (a) and the corresponding isotopic fractionation ($\Delta^{66}Zn_{adsorbed\text{-}aqueous}$) (b) with respect to different reaction time. Experiments were performed at a total Zn concentration of 0.2 mM at pH 6 at room temperature.

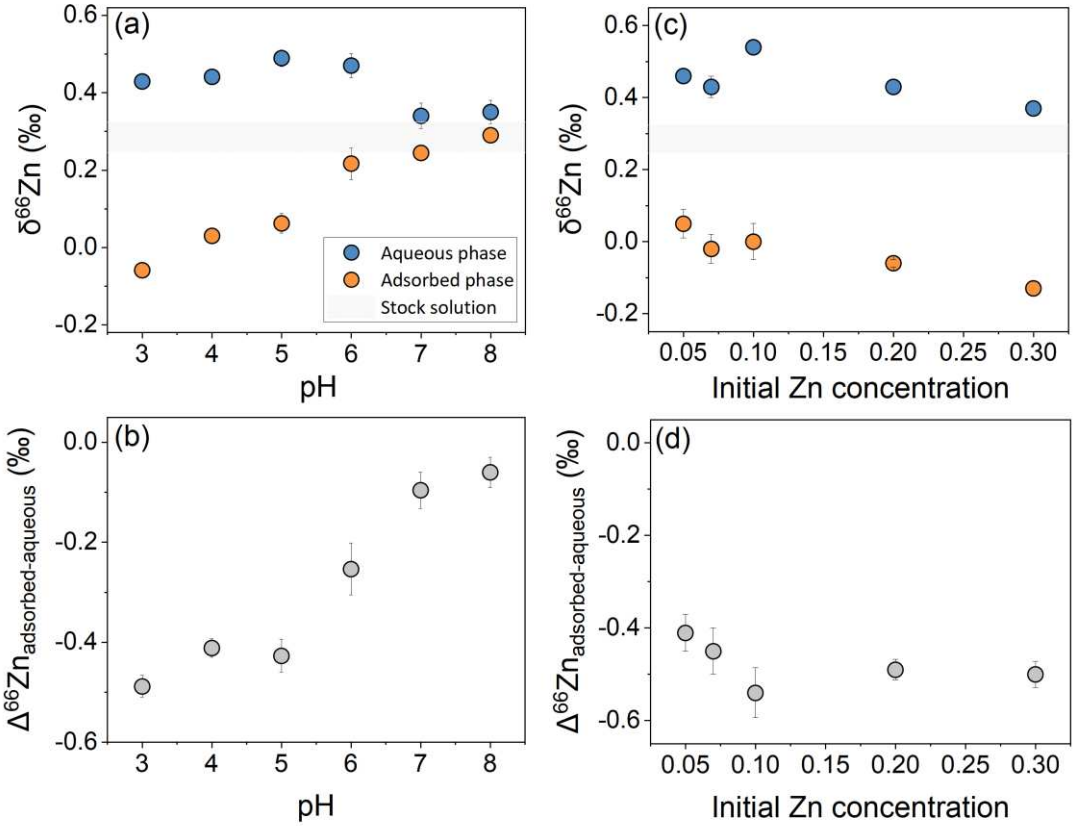

433

434

435 **Fig. 5** Isotopic compositions and isotopic fractionation of Zn for adsorption edge
436 experiments at a total Zn concentration of 0.2 mM (a, b) and for adsorption isotherm
437 experiments at pH 3 (c, d).

438

439

440 **3.4 Zinc bonding structure as determined by EXAFS**

441 The k^3-weighted EXAFS spectra of the Zn-birnessite samples and four Zn reference
442 compounds (i.e., chalcophanite ($ZnMn_3O_7 \cdot 3H_2O$, a reference for octahedral Zn (^{VI}Zn) on
443 birnessite), tetrahedral Zn (^{IV}Zn) on birnessite, hydrozincite ($Zn_3(OH)_6(CO_3)_2$)), and Zn
444 hydroxide ($Zn(OH)_2$) are shown in Fig. 6a. Chalcophanite consists of layered edge-sharing

445 Mn^{4+}–O octahedra, where one in seven octahedra are vacancies (Post and Appleman, 1988).
446 In chalcophanite, Zn octahedrally coordinated to three O atoms of Mn vacancies and three
447 O atoms of interlayer waters (Fig. 1b). In the reference compound ^{IV}Zn on birnessite, Zn is
448 coordinated to three O atoms of the Mn vacancy and one water molecule (Fig. 1a)
449 (Manceau et al., 2002). For Zn hydroxide and hydrozincite, Zn exists in tetrahedral
450 coordination and in both tetrahedral and octahedral coordination to O atoms in polymerised
451 forms, respectively (Ghose, 1964; Christensen, 1969).

452 The EXAFS oscillations of three samples prepared for Zn concentrations of 0.05−0.2
453 mM at pH 3 are similar to those of chalcophanite (Fig. 6a). Correspondingly, Fig. 6b shows
454 the Fourier transformed spectra (phase shift uncorrected) of the three samples, where two
455 main peaks are observed. These two peaks can be assigned to O and Mn backscattering
456 based on the structure of chalcophanite. Shell-by-shell fitting results are shown in Table 2,
457 showing first-shell Zn−O bond distances of 2.03−2.04 Å and 2.15−2.18 Å. These distances
458 are in good agreement with those expected for the distorted octahedra of Zn on birnessite,
459 where Zn coordinates one side to three O atoms of the Mn vacancy (2.01−2.02 Å) and on
460 the other side to three H_2O molecules (2.15−2.16 Å) (Manceau et al., 2002). The second
461 shell fitting returns a Zn-Mn distance of 3.50−3.52 Å and coordination numbers of 6.3−7.7,
462 which are consistent with the coordination of Zn as the TCS complex (Fig. 1b) above Mn
463 vacancies in birnessite sheets (e.g., Drits et al., 1997; Toner et al., 2006). This configuration
464 involves coordination of Zn to three O atoms at the Mn vacancy, which are shared by 6 Mn

atoms surrounding the vacancy, as occurs in chalcophanite. Previous work also found TCS tetrahedral Zn on vacancies, indicated by relatively shorter Zn−O (~1.97 Å) and Zn−Mn (~3.35 Å) interatomic distances (Marcus et al., 2004; Hinkle et al., 2017), which was not observed in our samples.

In contrast, the samples prepared for Zn concentration of 0.2 mM at pH 6 and pH 8 exhibit slightly different features, with a "beat" pattern weakened at higher k between 7 and 8.5 $Å^{-1}$. This suggests that either the adsorption site or the bonding geometry of Zn complexes varies with Zn surface coverage (Fig. 6a). The beat patterns of the spectra prepared at pH 6 and 8 are obviously different from those of Zn hydroxide ($Zn(OH)_2$) and hydrozincite ($Zn_5(CO_3)_2(OH)_6$) (Fig. 6a), indicating that polymerizing Zn as either Zn hydroxide or hydrozincite is highly unlikely. Thus, only Zn surface complexes on birnessite are considered in our systems. In the R-space, the first Zn-O shell shifts to lower values, indicating that the average Zn-O bond length ($R_{Zn\text{-}O}$) decreases. Significantly lower amplitudes of the second shell for the Zn−Mn pair are observed. This low amplitude indicates a lower proportion of Mn near-neighbors per Zn adsorbed on birnessite. The fit of the first shell is employed using two sets of Zn-O shells, one corresponding to octahedral Zn (^{VI}Zn-O) and the other to tetrahedral Zn (^{IV}Zn-O). Such a two-shell fitting approach has been successfully used in previous studies (Lefkowitz and Elzinga, 2015). The fit yields a bond length for ^{IV}Zn-O of 2.01−2.04 Å and for ^{VI}Zn-O of 2.17−2.18 Å (Table 2). These two-shell fit results are consistent with those of Manceau et al. (2002), who reported radial

485 distances for ^{IV}Zn−O in the range of 1.97-2.02 Å and for ^{VI}Zn-O in the range of 2.15−2.20
486 Å. Despite clear first-shell evidence for two Zn-adsorbed species, the second shell could
487 be well fitted using a single Zn−Mn pair, and the fit was not improved by the addition of a
488 second Zn–Mn pair. This fit yields an interatomic distance for Zn−Mn of 3.49 Å and CN
489 of 3.5. This second shell Zn-Mn distance of 3.49 Å is consistent with the coordination of
490 Zn as triple-corner-sharing complexes above Mn vacancies (Manceau et al., 2002; Hinkle
491 et al., 2017). The fitted CN of 3.5 is much smaller, however, than the CN values of 6 in
492 triple-corner-sharing complexes above Mn vacancies. Previous studies have shown that the
493 formation of bidentate corner-sharing and edge-sharing (i.e., DCS and DES) complexes of
494 metals (e.g., Pb, Ni and Zn) at birnessite edge sites results in CN values of ~2 (Villalobos
495 et al., 2005; Simanova et al., 2015). DES Zn complexes are unlikely to form because Zn is
496 observed to exist in octahedral coordination (average R_{Zn-O}: ~2.15 Å) based on our DFT
497 calculation (Fig. 7; Table 3), and the formation of DES octahedral Zn complexes
498 contradicts the relatively short Zn-O length. We thus propose that the Zn–Mn interatomic
499 distance, 3.49 Å, is a weighted average between TCS octahedral and DCS tetrahedral Zn
500 complexes. The relatively large Debye-Waller factor σ^2 of the second shell Zn-Mn
501 correlation (0.015 Å^2, Table 2) also indicates that more than one Zn–Mn pair is present in
502 the second shell.
503

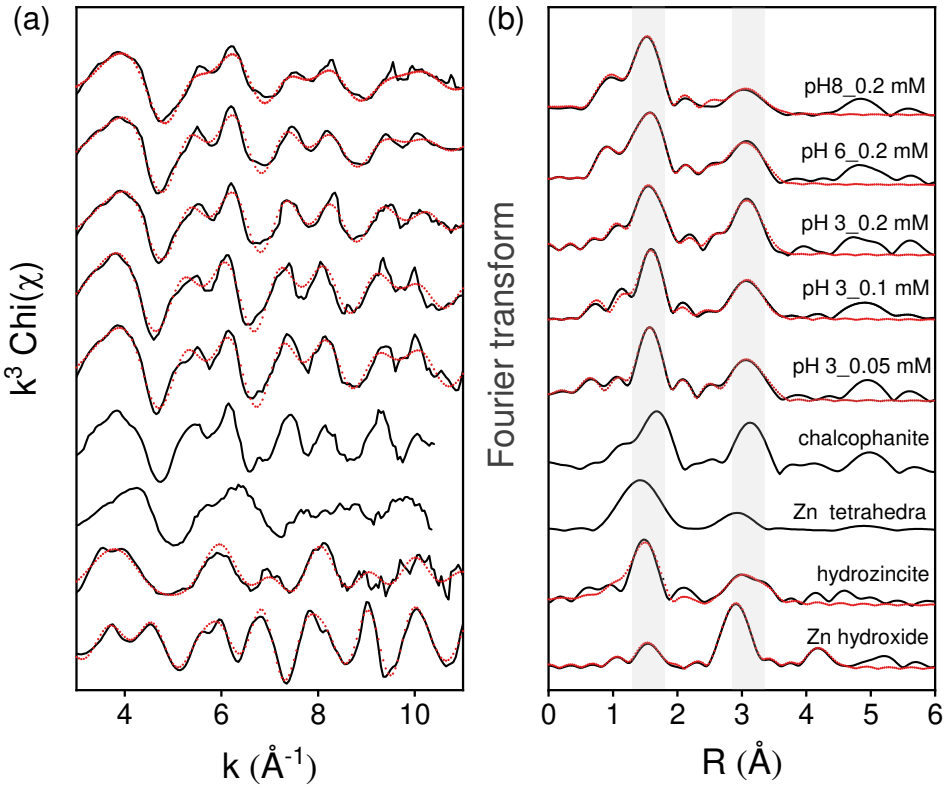
(a)
(b)
k3 Chi(χ)
Fourier transform
pH8_0.2 mM
pH 6_0.2 mM
pH 3_0.2 mM
pH 3_0.1 mM
pH 3_0.05 mM
chalcophanite
Zn tetrahedra
hydrozincite
Zn hydroxide
4
6
8
10
k (Å-1)
0
1
2
3
4
5
6
R (Å)

504

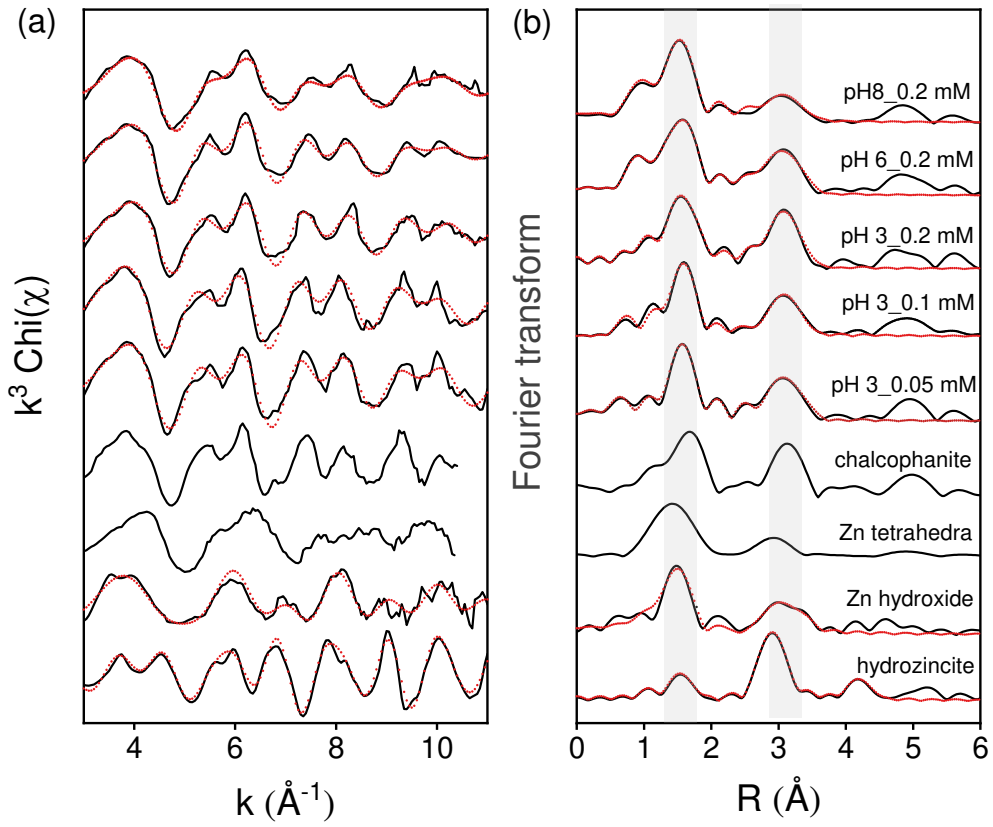

Fig. 6 (a) k^3-weighted EXAFS spectra of the Zn-birnessite samples and model compounds; (b) corresponding Fourier transforms in R space. Black solid lines and red dotted lines depict experimental and fitting data, respectively. Chalcophanite and Zn tetrahedra are two reference standards representing octahedral and tetrahedral Zn environment adsorbed on birnessite vacancies (Manceau et al., 2002).

3.5 Geometry optimization of Zn surface species

Geometry-optimized structures of Zn surface species are presented in Fig. 7 and Table 3. At the vacancy site, Zn formed octahedral or tetrahedral coordination depending on hydrating H_2O molecules (Fig. 7a and b). Octahedral Zn TCS shows larger Zn-O and Zn-Mn distances than tetrahedral Zn TCS (Table 3), which is consistent with previous work

517 (Post and Appleman, 1988; Manceau et al., 2002) and current EXAFS results (Table 2). At
518 the lateral edge sites, however, we are not able to obtain six-fold coordinated DCS
519 complexes. During the geometry optimization of the initial six-fold coordinated Zn DCS
520 model (i.e., Zn·4H_2O in Table 3), two H_2O molecules leave the initially coordinating Zn
521 cation and move to surface OH to form H-bonds with H_2O and surface OH (Fig. 7c),
522 resulting in four-fold coordinated Zn DCS, just as in the geometry optimization of the
523 Zn·2H_2O DCS model (Fig. 7d). The structural parameters of the Zn·4H_2O DCS model are
524 similar to those of the Zn·2H_2O DCS model. In a recent DFT-based molecular dynamics
525 study of hexaaquo-zinc complexes, the GGA-PBE method that we use in this study favors
526 tetraaquo- and pentaaquo-zinc complexes, and a van der Waals correction method such as
527 DFT–D (McNellis et al., 2009) is required to obtain a hexaaquo-zinc complex, as observed
528 in experiments (Ducher et al., 2017). We further geometrically optimized the initial sixfold
529 coordinated Zn·4H_2O DCS model using a DFT–D method; however, the DFT–D method
530 also predicts four-fold coordinated Zn DCS, similar to GGA-PBE (Table 3). In general, the
531 fully occupied 3*d* state of Zn^{2+} does not allow highly asymmetric coordination with
532 octahedral ligands and instead favors symmetric coordination, unlike transition metal
533 cations, whose 3*d* states are partially occupied (Jensen, 2003). Therefore, at the lateral edge
534 sites, octahedral Zn-DCS coordinated with two surface O and four water O atoms may be
535 electronically unstable to form. On the other hand, DES complexes exhibit six-fold
536 coordination regardless of whether Zn is coordinated with double-coordinated O or triply

coordinated O, and the *d*(Zn-O) is similar to the *d*(Zn-O) of octahedral Zn TCS.

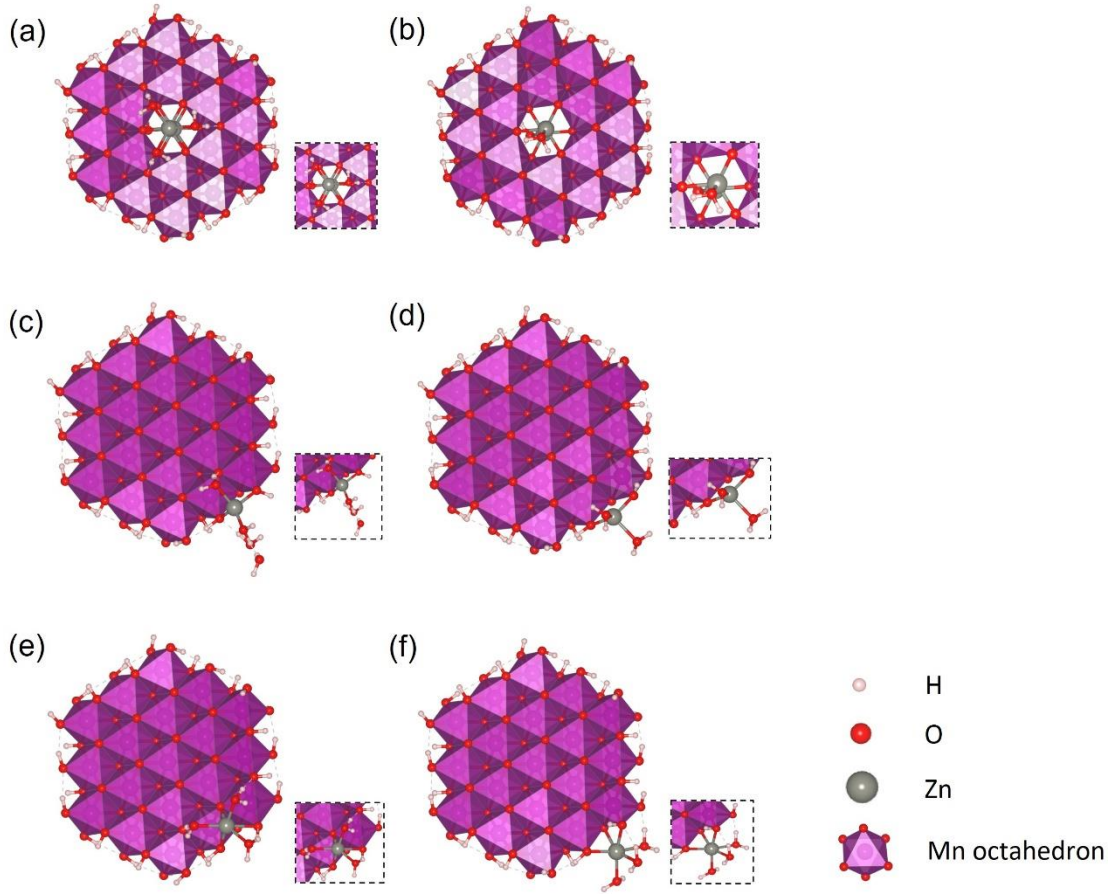

Fig. 7. DFT geometry-optimized (a) $Zn{\cdot}3H_2O$ and (b) $Zn{\cdot}1H_2O$ TCS complex models, (c) $Zn{\cdot}4H_2O$ and (d) $Zn{\cdot}2H_2O$ DCS complex models, and (e) $Zn{\cdot}3H_2O$ (with doubly coordinated oxygen) and (f) $Zn{\cdot}3H_2O$ (with triply coordinated oxygen) DES complex models formed at a birnessite nanodisk. The insets are the magnification of the interested area. See Table 3 for the structural parameters of each model.

3.6 Surface complexation modeling

Based on the results from EXAFS spectroscopy and DFT geometry optimization, metals can bind to both the interlayer vacancies and external edges of birnessite, and the surface speciation of Zn on birnessite is TCS complex on vacancies and DCS complex on edges. The surface adsorption reactions of Zn are thus described as follows:

Zn complex at internal surfaces:

$3 \equiv Mn_2O^{-2/3} + Zn^{2+} = (\equiv Mn_2O)_3Zn^0 \quad \log K_{TCS}$

Zn complex at external edges:

$2 \equiv MnOH^{-1/3} + Zn^{2+} + H_2O = (\equiv MnOH)_2ZnOH^{+1/3} + H^+ \quad \log K_{DCS}$

The best-fit model parameters are summarized in Table 4. The fitting results using two different species, $(\equiv Mn_2O)_3Zn^0$ and $(\equiv MnOH)_2ZnOH^{+1/3,}$ for the adsorption edge experiments in 0.1 M $NaNO_3$ solution are shown in Fig. 8. The results show that $(\equiv Mn_2O)_3Zn^0$ is the dominant surface species, particularly at low pH values of 3 to 5, which is consistent with previous work showing that vacancy sites play a dominant role in binding metal ions due to their highly negative charge (e.g., Toner et al., 2006; Kwon et al., 2009; Wang et al., 2018). The proportion of $(\equiv MnOH)_2ZnOH^{+1/3}$ increases from 4.4% at pH 6 to 36.2% at pH 8, suggesting that edge sites become important under alkaline conditions (Wang et al., 2018; Li et al., 2020). In general, for Zn on birnessite, the model describes a two-step adsorption trend with increasing pH.

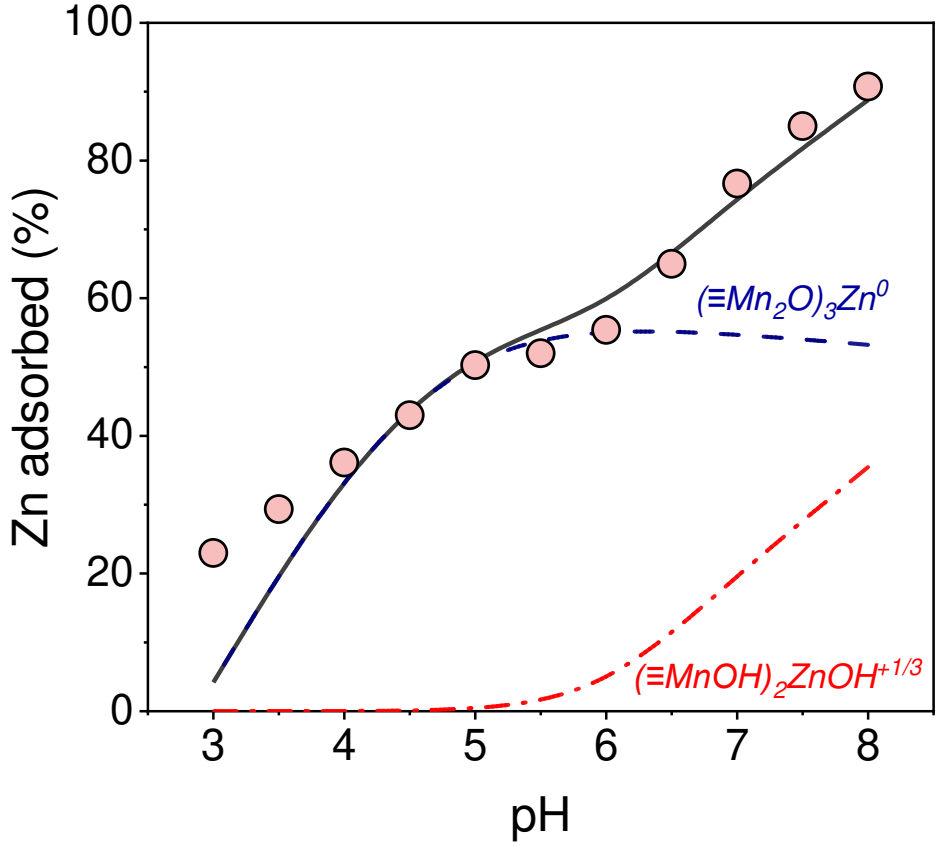

Fig. 8 Experimental (pink points) and calculated (black line) Zn adsorbed on birnessite as a function of pH in 0.1 M $NaNO_3$ solution. The model was fit based on the parameters in Table 3. The calculated Zn resulted from various proportions of Zn on the birnessite internal surface (blue dashed line) and Zn on the birnessite external surface (red dotted line).

4. Discussion

4.1 Constraining the equilibrium fractionation factors of Zn

Zn isotopes show different fractionation behaviour according to pH values for the adsorption edge experiments (Fig. 5a). Light Zn isotopes are observed to adsorb on the

birnessite surface, with $\Delta^{66}Zn_{adsorbed\text{-}aqueous}$ ranging from -0.54 ± 0.05‰ to -0.06 ± 0.04‰. An equilibrium fractionation process can better describe the evolution of Zn isotopic compositions, while a Rayleigh process is rejected (detailed in Fig. S3). In this process, two distinct fractionation factors are involved: one for low pH values when Zn adsorption is low and predominantly onto vacancy sites and the other for higher pH values when Zn adsorption is higher and onto edge sites. For different pH values, the distinct isotopic signatures of adsorbed Zn therefore result from different amounts of Zn adsorbed and different proportions of vacancy and edge Zn species. The Zn isotopic fractionation factor can be determined for each Zn species based on the changes in $\delta^{66}Zn_{adsorbed}$ with pH.

In the experiments in the pH range 3 to 5, an average $\Delta^{66}Zn_{adsorbed\text{-}aqueous}$ of -0.46 ± 0.06‰ is observed. According to our EXAFS, at low pH values, only vacancy sites contribute to Zn binding (Fig. 6). The isotopic fractionation factor for Zn adsorption as TCS octahedral surface complexes on vacancy sites is thus the value that we measured ($\Delta^{66}Zn_{TCS\text{-}aqueous}$ = -0.46 ± 0.03‰; Table 1). In adsorption experiments in the pH range of 6 to 9, isotopic fractionation magnitudes significantly decrease from -0.43 ± 0.03‰ to -0.09 ± 0.05‰. As indicated by both the EXAFS results, at higher pH values (e.g., pH 8), binding to edge sites appears and becomes increasingly important (Fig. 6). Vacancy site and edge site adsorption both contribute to the measured Zn isotopic fractionation at high pH values. A $\Delta^{66}Zn_{adsorbed\text{-}aqueous}$ of -0.06 ± 0.05‰ is observed at pH 8 (Fig. 5), and the model predicts 39.9% Zn binding on edge sites and 59.9% Zn binding on vacancy sites (Fig. 8). Thus we

calculated the isotopic fractionation value for Zn adsorption as DCS tetrahedral surface complexes on edge sites based on a two end–member mixing equation:

$$\Delta^{66}Zn_{adsorbed-aqueous} = \Delta^{66}Zn_{TCS-aqueous} * p_{TCS} + \Delta^{66}Zn_{DCS-aqueous} * p_{TCS} \quad (4)$$

where p_{TCS} and p_{DCS} are the respective proportions of vacancy and edge sites involved, and $\Delta^{66}Zn_{DCS\text{-}aqueous}$ is the estimated isotopic fractionation value for Zn adsorption onto edge sites. The Zn isotopic fractionation factor associated with edge sites is thus $\Delta^{66}Zn_{DCS\text{-}aqueous}$ = 0.52 ± 0.03‰. We chose the sample obtained at pH 8 to calculate $\alpha_{DCS\text{-}aqueous}$ because the EXAFS spectrum (Fig. 6) confirms that Zn adsorbed on both the vacancy and edge sites of birnessite at pH 8, and the surface complexation modeling (Fig. 8) fits the experimental data at pH 8 very well.

The theoretical $\delta^{66}Zn_{aqueous}$ is calculated to verify the correctness of the two fractionation factors when both binding sites are involved during adsorption:

$$\delta^{66}Zn_{aqueous} = \delta^{66}Zn_{stock} - 1000f\left(\frac{p_{TCS}(\alpha_{TCS-aqueous}-1)}{1-f+(f*\alpha_{TCS-aqueous})} + \frac{p_{DCS}(\alpha_{DCS-aqueous}-1)}{1-f+(f*\alpha_{DCS-aqueous})}\right) \quad (5)$$

where $\alpha_{TCS\text{-}aqueous}$ and $\alpha_{DCS\text{-}aqueous}$ are the isotopic fractionation coefficients associated with vacancy and edge sites, respectively. The corresponding $\delta^{66}Zn_{adsorbed}$ on the birnessite surface is calculated from equation (6) as:

$$\delta^{66}Zn_{adsorbed} = \delta^{66}Zn_{aqueous} + \Delta^{66}Zn_{TCS-aqueous} * p_{TCS} + \Delta^{66}Zn_{DCS-aqueous} * p_{DCS} \quad (6)$$

Fig. 9a shows the theoretical calculations of $\delta^{66}Zn_{adsorbed}$ and $\delta^{66}Zn_{aqueous}$ when both binding sites contribute to Zn adsorption. The dashed line separates the fraction of Zn adsorbed as

TCS octahedral surface complexes on vacancy sites (pink area) from those adsorbed as DCS tetrahedral surface complexes on edge sites (blue area). The theoretical $\delta^{66}Zn_{adsorbed}$ and $\delta^{66}Zn_{aqueous}$ are in good agreement with the measured Zn isotope compositions in the adsorption edge experiments. The agreement between the theoretical calculations based on the isotopic fractionation coefficients and the experimental results (Fig. 9) indicates the robustness of the two Zn isotopic fractionation factors that we propose for Zn adsorption on birnessite vacancies and edge sites. Furthermore, this good agreement between the theoretical $\delta^{66}Zn$ based on our surface complexation model and the measured $\delta^{66}Zn$ supports the evidence of control by vacancy sites at low pH and the contribution from both the vacancy and edge sites at high pH.

In adsorption isotherm experiments at pH 3, the experimental data are better fitted by the equilibrium fractionation model than by the Rayleigh model (Fig. 9b and Fig. S3). This equilibrium fractionation process is consistent with previous studies on Zn fractionation caused by adsorption on various minerals (e.g., Wasylenki et al., 2014; Wang et al., 2022). Regression yields an $\alpha_{adsorbed\text{-}aqueous}$ factor of 0.99953, which is consistent with the result ($\alpha_{TCS\text{-}aqueous}$ = 0.99954) for Zn adsorption on vacancy sites. The consistency between the $\alpha_{adsorbed\text{-}aqueous}$ factor for adsorption isotherm experiments at pH 3 and $\alpha_{TCS\text{-}aqueous}$ for Zn adsorption on vacancy sites is in accordance with our EXAFS results, which shows that the vacancy sites contribute exclusively to Zn adsorption at low pH.

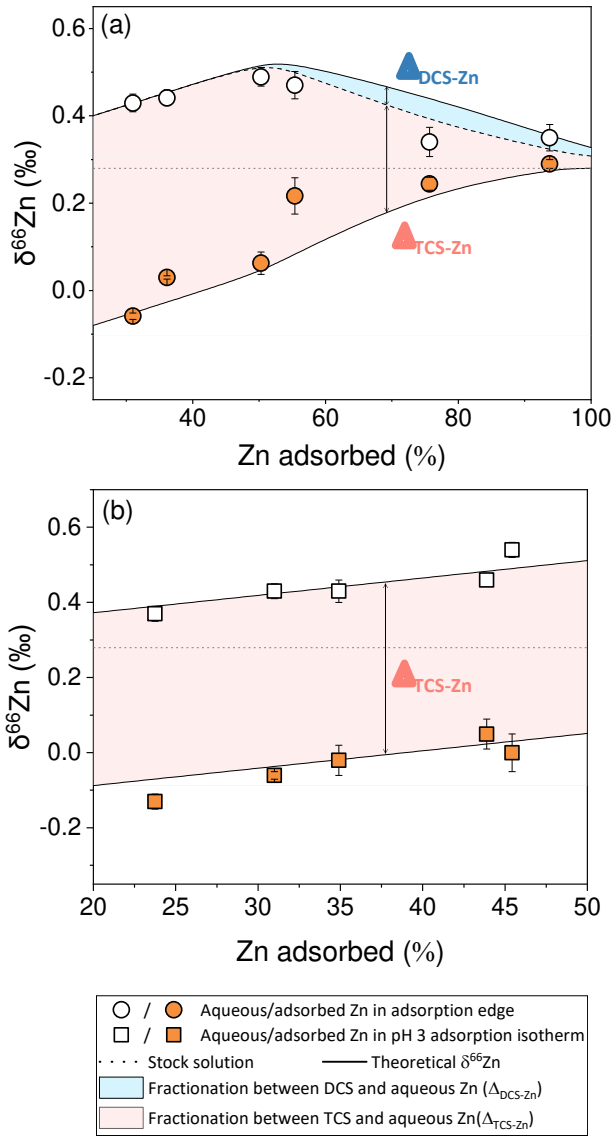

Fig. 9. Aqueous and adsorbed Zn isotopic compositions with respect to the fraction of Zn (a) for 0.2 mM adsorption edge experiments and (b) for pH 3 adsorption isotherm experiments. The dotted line depicts the Zn isotopic composition of the stock solution. Error bars are 2 SD from 3 replicate analyses. Solid lines show the theoretical evolution of $\delta^{66}Zn_{adsorbed}$ and $\delta^{66}Zn_{aqueous}$ based on the two-site model. The dashed line separates the fraction of $\Delta^{66}Zn_{adsorbed\text{-}aqueous}$ explained by Zn adsorption as TCS surface complexes on vacancy sites (pink area) or DCS surface complexes on edge sites (blue area).

4.2 Site-specific Zn structure controls isotopic fractionation

The different isotopic fractionation magnitudes of Zn at low and high pH (Fig. 10) can be interpreted by the differences in adsorption complex structures of Zn on various birnessite reactive sites because such differences in the bonding environments lead to changes in Zn-O bond strength (Schauble, 2004). According to stable isotope theory, heavy isotopes prefer to exist in stronger bonding environments (e.g., lower coordination numbers) (Bigeleisen and Mayer, 1947; Schauble, 2004).

The TCS octahedral Zn complexes at pH 3 on birnessite vacancy sites concentrate light Zn relative to the solution($\Delta^{66}Zn_{TCS\text{-}aqueous}$ ~ -0.46 ± 0.04‰) (Fig. 10). The octahedral complexes of Zn on birnessite indicate that the coordination number of aqueous Zn does not change during adsorption; however, significant isotopic fractionation occurs. Our EXAFS results show that the Zn octahedra on birnessite are distorted, with each Zn coordinate on one side to three oxygen atoms of the Mn vacancy (bond length: 2.03–2.04 Å) and on the other side to three H_2O molecules (bond length: 2.15–2.18 Å) (Table 2). Metal-oxygen polyhedral distortion is proposed as a factor driving isotopic fractionation (Nakada et al., 2017; Wasylenki et al., 2014; Yan et al., 2021). For example, the distorted structures of Ce-O coordination are speculated to be the main reason for the enrichment of light isotope on δ-MnO_2 (Nakada et al., 2017). Similarly, light Cd isotopes enriched in birnessite with the formation of a distorted Cd-O octahedron is observed (Wasylenki et al., 2014; Yan et al., 2021). In our Zn-birnessite system, the formation of Zn-O distorted

octahedra on vacancy sites might lead to the enrichment of light Zn. In accordance with theoretical predictions, because an average Zn-O bond length of ~2.09 Å is obtained, this longer bond length relative to aqueous Zn (~2.06 Å) should lead to a weaker Zn-O bond and thus preferential enrichment of light Zn isotopes on birnessite.

In this study, DCS complexes of Zn on birnessite edge sites occur at higher pH values (6 to 9), and Zn adsorption on edge sites induces isotopic fractionation of $\Delta^{66}Zn_{DCS\text{-}aqueous}$ ~ 0.52 ± 0.04‰ (Fig. 10). The fractionation factor of $\Delta^{66}Zn_{DCS\text{-}aqueous}$ of 0.52 ± 0.04‰ seems to be comparable to those observed for Zn adsorption onto several different minerals (e.g., Juillot et al., 2008; Guinoiseau et al., 2016). Juillot et al. (2008) found that tetrahedral Zn forms on ferrihydrite, yielding a fractionation factor of $\Delta^{66}Zn_{adsorbed\text{-}aqueous}$ of 0.52 ± 0.04‰. Similarly, a recent study found that tetrahedral Zn forms on Al oxide, leading to a $\Delta^{66}Zn_{adsorbed\text{-}aqueous}$ fractionation of 0.49 ± 0.06‰ (Gou et al., 2018). In these two systems, lower coordination numbers (CN: 4) with shorter Zn-O bond lengths ($R_{Zn\text{-}O}$: ~1.96 Å) relative to aqueous Zn (CN: 6, $R_{Zn\text{-}O}$: ~2.06 Å) were observed, which should induce a stronger Zn−O bond for Zn adsorption, thus concentrating heavy Zn isotopes. It is noteworthy that the adsorption of Zn to amorphous SiO_2 surfaces results in a much greater Zn isotope fractionation ($\Delta^{66}Zn_{adsorbed\text{-}aqueous}$ ~ 0.8−1.2‰) (Nelson et al., 2017). In this case, for amorphous SiO_2, EXAFS data show a tetrahedral complex but with a particularly short Zn−O bond length (~1.93 Å). In contrast, although a similar Zn isotope fractionation ($\Delta^{66}Zn_{adsorbed\text{-}aqueous}$ ~ 0.49 ± 0.06‰) during adsorption is reported for kaolinite (Guinoiseau

et al., 2016), Zn is observed to exist in octahedral coordination at the kaolinite surface, with a Zn−O distance (2.07 Å) similar to that of aqueous Zn (2.06 Å) (Nachtegaal and Sparks, 2004). In the kaolinite system, the CN and Zn-O bond lengths appear to remain unchanged during Zn adsorption. The significant isotopic fractionation without a change in coordinated structure (i.e., CN and R_{Zn-O}) is likely due, however, to a mismatch between the isotopic fractionation and EXAFS spectra because EXAFS measurements are performed at a much higher Zn concentration, and only one sample is analyzed (Nachtegaal and Sparks, 2004; Guinoiseau et al., 2016). Unfortunately, additional EXAFS studies are not available to further constrain the fractionation mechanism of Zn isotope fractionation caused by adsorption on kaolinite. In our Zn-birnessite system, although we do not experimentally obtain the end-member structure of DCS complexes of Zn on birnessite, DCS Zn complexes always form along with TCS Zn complexes and the shorter EXAFS-derived Zn-O bond distances of the mixed DCS and TCS octahedral Zn (as opposed to exclusively octahedral Zn), and DFT calculations of Zn-DCS both confirm that DCS Zn exists in tetrahedral coordination (Fig. 6, Table 3). This formation of DCS tetrahedral Zn with shorter Zn-O length (1.97-1.98 Å) relative to aqueous Zn (~2.06 Å) seems to be responsible for the observed isotopic fractionation during Zn adsorption to the edge sites of birnessite.

At a given temperature and pressure, equilibrium isotopic fractionation factors of an element are theoretically predicted to be controlled by the relative bond strengths between

706 that element and its coordinating atoms (Bigeleisen and Mayer, 1947; Schauble, 2004),
707 which are jointly determined by multiple factors, including bond length, coordination
708 number, oxidation state and electronic configuration (Schauble et al., 2004; Young et al.,
709 2009). In general, longer bond lengths correspond to weaker bond strengths and have lower
710 vibrational frequencies, and thus elements in longer bonding environments should prefer
711 to incorporate lighter isotopes relative to those in shorter bonding environments. A
712 correlation between the average Zn–O bond lengths obtained from EXAFS spectroscopy
713 and their corresponding isotopic fractionation magnitudes caused by adsorption on a
714 variety of different mineral surfaces (Fig. 11) suggests that there is a general rule that Zn–
715 O bond lengths impart a first-order control on Zn isotope fractionation. Specifically, the Zn
716 with the longest Zn−O bond distance (2.10 ± 0.02 Å) is related to the enrichment of the
717 lightest Zn isotopes ($\Delta^{66}Zn_{adsorbed\text{-}aqueous}$ = ~ -0.46‰), while the Zn with the shortest Zn−O
718 length (1.93 Å) is related to the enrichment of the heaviest Zn ($\Delta^{66}Zn_{adsorbed\text{-}aqueous}$ = ~
719 0.8−1.2‰). In the work here Zn-O bond length is interpreted as a function of tetrahedral
720 vs octahedral complex, but in addition the extended bonding environment around adsorbed
721 Zn may also influence the first shell bond length, especially for Zn adsorption onto different
722 minerals.
723
724

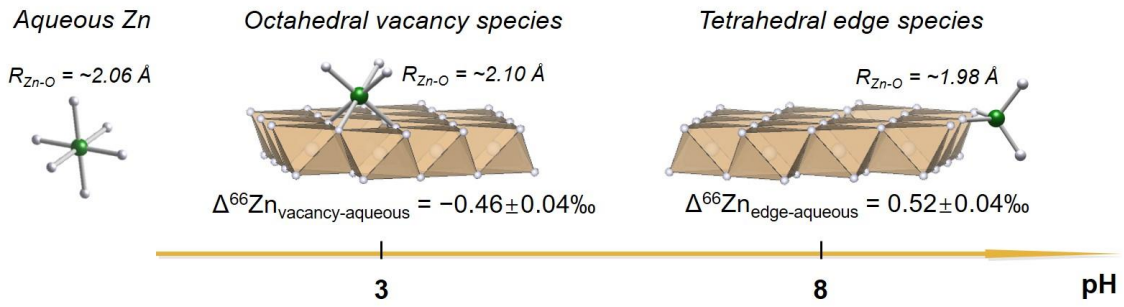

725
726 **Fig. 10.** Schematic representation of site-specific Zn isotopic fractionation caused by
727 adsorption on birnessite and the dominant Zn species on birnessite at different pH values.
728
729

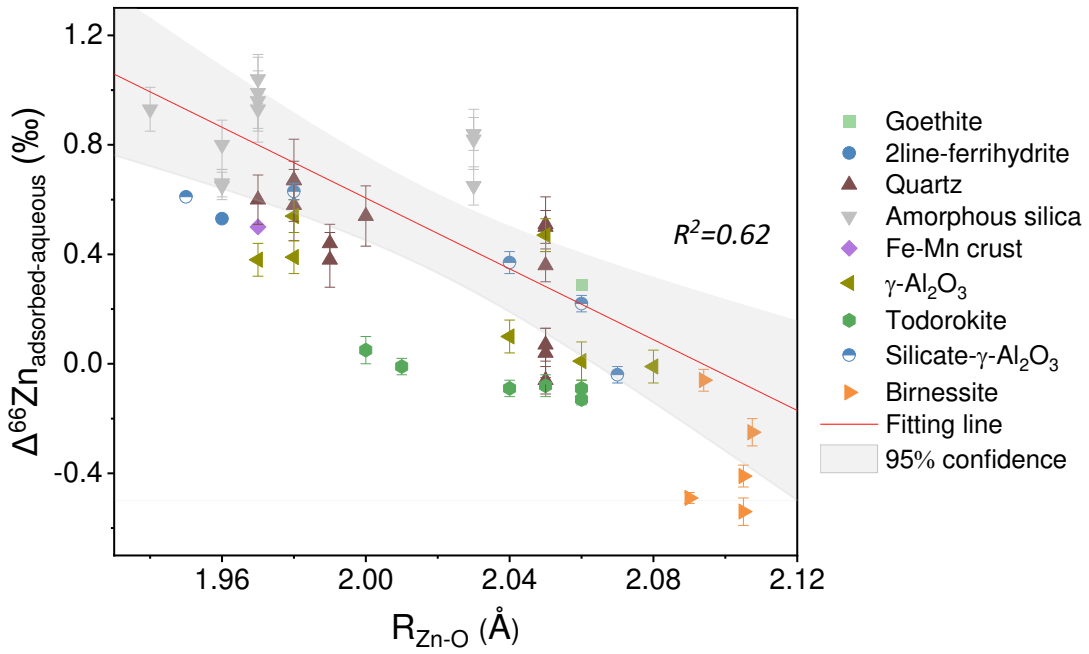

730
731 **Fig. 11.** Correlation of isotopic fractionation ($\Delta^{66}Zn_{adsorbed-aqueous}$) caused by sorption to various
732 minerals and the associated structural chemistry parameters (i.e., R_{Zn-O}). Plotted data refer to
733 those reported previously for goethite (Juilot et al., 2008), 2-line ferrihydrite (Juilot et al., 2008),
734 quartz (Nelson et al., 2017), amorphous silica (Nelson et al., 2017), Fe-Mn nodules (Little et al.,
735 2014a), γ-Al_2O_3 (Gou et al., 2018), todorokite (Wang et al., 2022), silicate-γ-Al_2O_3 (Gou et al.,
736 2022), and birnessite (this study). The solid red fitting line was obtained by linear regression
737 analysis. The gray area depicts the 95% confidence band. The error bars represent an analytical
738 uncertainty of 2 SD.
739
740 **4.3 Implications for understanding Zn isotope fractionation in natural birnessite-**

containing settings

Birnessite is a major mineral phase in freshwater (Manceau et al., 2007) and many soils (Hochella et al., 2005; Lanson et al., 2008), as well as an important component in marine sediments and ferromanganese crusts (Post, 1999; Bodei et al., 2007). It is also commonly found as a secondary product in metal ore deposits (Post, 1999; Spinks and Uvarova, 2019). Due to its unusually high adsorption capacities and scavenging capabilities, birnessite readily participates in adsorption and oxidation–reduction reactions and therefore provides one of the primary controls on trace metal cycling in Earth's surface environments (Post, 1999; Peacock and Sherman, 2007b; Atkins et al., 2016).

Zinc, as an important micronutrient required by organisms (Sinoir et al., 2012) and at elevated concentrations a toxic contaminant (Sandstead, 2014), has been shown to commonly coexist with birnessite in natural environments, such as acid mine drainage sites, soils, and marine sediments (Kay et al., 2004; Mayanna et al., 2015). Zinc isotopes may fractionate during environmental interactions with birnessite (e.g., Bryan et al., 2015). In this study, we show that light Zn isotopes are preferentially adsorbed on birnessite surfaces, with a fractionation factor of $\Delta^{66}Zn_{adsorbed-aqueous}$ = -0.46 ± 0.04‰ at acidic pH and a low Zn/Mn molar ratio (0.037–0.170) compared to a less fractionation factor ($\Delta^{66}Zn_{adsorbed-aqueous}$ ~ -0.09 ± 0.04‰) at circumneutral pH and a high Zn/Mn molar ratio (0.170–0.327) (Fig. 12). Combining our results with those in the literature, however, we can chart and predict the evolution of Zn isotope fractionation with Zn speciation as a function of pH and

761 Zn/Mn molar ratio (Manceau et al., 2002; Grangeon et al., 2012) (Fig 12). Specifically, in
762 hydrogenetic marine Mn crusts (birnessite as the main Mn mineral phase), pH and Zn/Mn
763 molar ratio appear to be decoupled, in that pH is high (pH~8) but Zn/Mn molar ratio is very
764 low (~0.004), yet Zn is reported to form TCS tetrahedral surface complexes on vacancy
765 sites of birnessite (Little et al., 2014a) with a fractionation between crusts and seawater of
766 ~0.5‰ (e.g., Marechal et al., 2000; Conway et al., 2013). This suggests that at low surface
767 coverage, the TCS tetrahedral complex on vacancy sites forms independently of pH
768 (vacancy tetrahdra V_{tet}, Fig. 12). However, as the surface coverage increases, Zn isotope
769 fractionation should decrease because of the formation of TCS octahedral Zn at higher
770 Zn/Mn ratios (Manceau et al., 2002) (V_{tet} and vacancy octahedra V_{oct}, Fig. 12). Then, at
771 higher surface coverage, we still observe that at Zn/Mn ratios from ~0.037 to ~0.170, light
772 Zn isotopes are adsorbed at the birnessite surface, with a fractionation factor $\Delta^{66}Zn_{adsorbed-}$
773 $_{aqueous}$ of ~-0.46‰ where Zn forms fully TCS octahedral complexes (V_{oct}, Fig. 12). Then,
774 as the surface coverage and pH further increase (i.e., 0.170<Zn/Mn <0.327, pH 6–9), we
775 observe that Zn isotope fractionation decreases with a fractionation factor $\Delta^{66}Zn_{adsorbed-}$
776 $_{aqueous}$ of ~ -0.09‰, where Zn exists in both TCS octahedral and DCS tetrahedral
777 coordination (V_{oct} and edge tetrahedra E_{tet}, Fig. 12). It should be noted that the exact pH
778 and Zn/Mn molar ratios correlating to the associated Zn end-member structures (i.e., TCS
779 tetrahedral V_{tet}, TCS octahedral V_{oct}, and DCS tetrahedral Zn E_{tet}), which are then used to
780 predict Zn isotope fractionation, may change with respect to different structural

781 characteristics of birnessite (e.g., quantity of Mn vacancies and Mn AOS) (Manceau et al.,
782 2002; Kwon et al., 2009; Yin et al., 2018), but this should not change the overall predicted
783 evolutionary trend of Zn isotope fractionation as a function of pH and Zn/Mn ratios.

784 Simplified conditions are used in the adsorption experiments (absence of multiple
785 ligands and a focus on one mineral phase), and Zn isotopic fractionation may be influenced
786 by complexation with different ligands and by adsorption to other mineral surfaces (e.g.,
787 Fe oxides) in natural environments (Fujii et al., 2014; Spinks and Uvarova, 2019). The
788 exact fractionation magnitudes of Zn caused by natural birnessite adsorption could thus be
789 either slightly smaller (e.g., as influenced by chloride complexation) (Fujii et al., 2014) or
790 larger (e.g., influenced by ferrihydrite adsorption) (Juillot et al., 2008) than the values from
791 our experiments. Therefore, in natural conditions, multiple factors, such as
792 organic/inorganic ligands, different mineral surfaces, and solution conditions, should be
793 taken into consideration when studying the fractionation magnitudes of Zn isotopes caused
794 by birnessite adsorption. It is apparent, however, that Zn isotope fractionation caused by
795 adsorption on birnessite is significant and should be carefully considered when using Zn
796 isotopes to investigate processes in natural Mn-bearing environments.
797
798

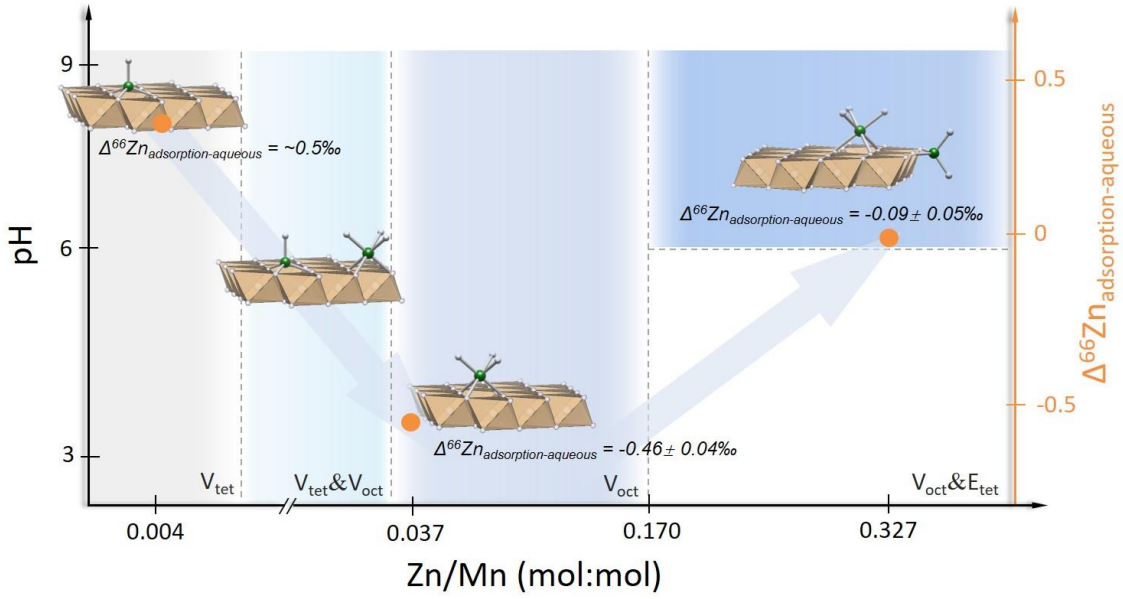

Fig. 12 Schematic illustration of the evolution of Zn speciation on birnessite and the predicted isotopic fractionation (orange circles) as a function of pH values and Zn/Mn molar ratios. Dashed lines and shaded areas are drawn based on Zn isotopic data and EXAFS spectroscopic analyses. V_{tet} and V_{oct} refer to triple-corner-sharing TCS Zn complexes, existing in tetrahedral and octahedral coordination on vacancy sites, respectively. E_{tet} refers to double-corner-sharing DCS tetrahedral Zn complexes on edge sites. The arrows depict the predicted trend of Zn isotope fractionation according to Zn speciation.

5. Conclusion

In this study, Zn isotope fractionation was quantified during adsorption onto synthetic birnessite. Additionally, we constrain the fractionation mechanisms by coupling EXAFS spectroscopy, DFT geometry optimisation, and SCM modeling. The results suggest that the adsorbed Zn exhibits a preferential enrichment of light isotopes, with $\Delta^{66}Zn_{adsorbed-aqueous}$ ranging from –0.46 ± 0.04‰ at low pH to –0.09 ± 0.05‰ at high pH. The change in Zn isotopic fractionation as a function of pH is described using a two-site adsorption model

where two binding sites are included: interlayer vacancies and external edge sites. According to this model, two distinct isotopic fractionation factors of Zn are calculated: $\Delta^{66}Zn_{adsorbed\text{-}aqueous}$ = -0.46 ± 0.04‰ for adsorption onto vacancy sites and $\Delta^{66}Zn_{adsorbed\text{-}aqueous}$ = 0.52 ± 0.04‰ for binding to edge sites. The site-specific Zn isotopic fractionation can be explained by the local structures of Zn at molecular-level. Zn adsorbs to the vacancy sites of birnessite in TCS octahedral coordination at low pH (average bond length: ~2.09 Å) with the enrichment of light Zn on birnessite. In contrast, Zn begins to form a DCS tetrahedral complex at higher pH values on edge sites at the birnessite surface with a calculated fractionation factor ($\Delta^{66}Zn_{adsorbed\text{-}aqueous}$) of 0.52 ± 0.04‰. We assert that differences in bonding structures result in the differences in isotopic fractionation factors for binding to different reactive sites of the birnessite surface, as TCS octahedral Zn formation on vacancy sites with a shorter bond length relative to DCS tetrahedral Zn on edge sites is associated with a lower vibrational frequency and thus incorporates lighter isotopes.

Site-specific isotopic fractionation is strongly dependent on solution pH, suggesting the importance of isotopic fractionation of Zn caused by adsorption on birnessite in natural environments with varying pH values. Because birnessite minerals are highly reactive and control the concentrations and speciation of various trace metals, notably Zn, in both terrestrial and marine environments (Post, 1999; Manceau et al., 2002; Koschinsky and Hein, 2003), the chemical conditions of birnessite-rich environments should be carefully

considered in any isotopic studies of biogeochemical cycling. Moreover, the site-specific reactivity of birnessite provided by Zn isotopes in this study offers new insights into the links between adsorption and fractionation, which can be useful for predicting the fractionation behavior of other similar metals.

Acknowledgments

This manuscript benefits from the constructive comments from the EIC, Prof. Jeffrey Catalano, the AE, Prof. Mélanie Davranche, Prof. Ryan Mathur, and two anonymous reviewers. We greatly appreciate the National Natural Science Foundation of China (NSFC) (Grant Nos. 41977267, 42011530177) and Fundamental Research Funds for the Central Universities-Nanjing University for this work. Both Caroline Peacock and Wei Li appreciate international collaborative research funding from the Royal Society (RS) Newton Mobility Grant and NSFC (IEC/NSFC/191423). Kideok Kwon acknowledges the support from the National Research Foundation of Korea, Republic of Korea (NRF) (NRF-2019R1A2C2084299). We thank Prof. Zhengrong Wang, Dr. Wenxian Gou, and Dr. Xinxin Mo for insightful discussion during manuscript preparation. Drs. Jing Zhang and Lirong Zheng are acknowledged for the assistance of EXAFS experiments at the Beijing Synchrotron Radiation Facility on 1W1B beamline. We appreciate Prof. Alain Manceau for providing Zn reference EXAFS spectra on birnessite.

Appendix A. Supplementary Material

The supplementary material for this article includes supplementary figures and a file of Research Data. Supplementary figures contains speciation of aqueous Zn (Figure S1), plots of the correlation between modeled and measured Zn adsorbed on birnessite (Figure S2), Equilibrium or Rayleigh fractionation model (Figure S3). The file of Research Data includes the raw data of Fig. 6 and 11.

References

Appelo, C. A. J. and Postma, D. (1999) A consistent model for surface complexation on birnessite (δ-MnO2) and its application to a column experiment. *Geochim. Cosmochim. Acta* **63**, 3039–3048.

Aranda S., Borrok D. M., Wanty R. B. and Balistrieri, L. S. (2012) Zinc isotope investigation of surface and pore waters in a mountain watershed impacted by acid rock drainage. *Sci. Total Environ.* **420**, 202-213.

Atkins A. L., Shaw S. and Peacock C. L. (2014) Nucleation and growth of todorokite from birnessite: implications for tracemetal cycling in marine sediments. *Geochim. Cosmochim. Acta* **144**, 109–125.

Atkins, A.L., Shaw, S. and Peacock, C.L. (2016). Release of Ni from birnessite during transformation of birnessite to todorokite: implications for Ni cycling in marine

876 sediments. *Geochim. Cosmochim. Acta* **189**, 158–183.
877 Balistrieri L. S., Borrok D. M., Wanty R. B. and Ridley W. I. (2008) Fractionation of Cu
878 and Zn isotopes during adsorption onto amorphous Fe(III) oxyhydroxide:
879 experimental mixing of acid rock drainage and ambient river water. *Geochim.*
880 *Cosmochim. Acta* **72**, 311–328.
881 Bargar J. R., Fuller C. C., Marcus M. A., Brearley A. J., Perez Dela Rosa M., Webb S. M.
882 and Caldwell W. A. (2009) Structural characterization of terrestrial microbial Mn
883 oxides from Pinal Creek, AZ. *Geochim. Cosmochim. Acta* **73**, 889–910.
884 Bi X. Y., Li Z. G., Wang S. X., Zhang L., Xu R., Liu J. L., Yang H. M. and Guo M. Z.
885 (2017) Lead isotopic compositions of selected coals, Pb/Zn ores and fuels in China
886 and the application for source tracing. *Environ. Sci. Technol*. **51**, 13502–
887 13508.Bigeleisen J. and Mayer M. G. (1947) Calculation of equilibrium constants for
888 isotopic exchange reactions. *J. Chem. Phys.* **15**, 261–267.
889 Bigeleisen J. and Mayer M. G. (1947) Calculation of equilibrium constants for isotopic
890 exchange reactions. *J. Chem. Phys*. **15**, 261–267.
891 Bodeı S., Manceau A., Geoffroy N., Baronnet A. and Buatier M. (2007) Formation of
892 todorokite from vernadite in Ni-rich hemipelagic sediments. *Geochim. Cosmochim.*
893 *Acta* **71**, 5698–5716.
894 Bryan A. L., Dong S., Wilkes E. B. and Wasylenki L. E. (2015) Zinc isotope fractionation
895 during adsorption onto Mn oxyhydroxide at low and high ionic strength. *Geochim.*

Cosmochim. Acta **157**, 182–197.

Chen, J., Gaillardet, J. and Louvat, P. (2008) Zinc isotopes in the Seine river waters, France: A probe of anthropogenic contamination. *Environ. Sci. Technol.* **42**, 6494−6501.

Christensen A. N. (1969) The crystal structure of c-Zn(OH)2. *Acta Chem. Scand*. **23**, 2016–2020.

Conway T. M., Rosenberg A. D., Adkins J. F. and John S. G. (2013) A new method for precise determination of iron, zinc and cadmium stable isotope ratios in seawater by double-spike mass spectrometry. *Anal. Chim. Acta* **793**, 44–52.

Dong S. and Wasylenki L. E. (2016) Zinc isotope fractionation during adsorption to calcite at high and low ionic strength. *Chem. Geol.* **447**, 70–78.

Drits V. A., Lanson B., Bougerol-Chaillout C., Gorshkov A. I. and Manceau A. (2002) Structure of heavy-metal sorbed birnessite: Part 2. Results from electron diffraction. *Am. Mineral.* **87**, 1646–1661.

Drits V. A., Silvester E., Gorshkov A. I. and Manceau A. (1997) Structure of synthetic monoclinic Na-rich birnessite and hexagonal birnessite; I, Results from X-ray diffraction and selectedarea electron diffraction. *Am. Mineral.* **82**, 946–961.

Ducher M., Pietrucci F., Balan E., Ferlat G., Paulatto L. and Blanchard M. (2017) van der Waals contribution to the relative stability of aqueous Zn2+ coordination states. J. Chem. *Theory Comput*. **13**, 3340–3347.

Feng X. H., Zhai L. M., Tan W. F., Liu F. and He J. Z. (2007) Adsorption and redox

916 reactions of heavy metals on synthesized Mn oxide minerals. *Environ. Pollut*. **147**,
917 366–373.
918 Feng X., Zhu M., Ginder-Vogel M., Ni C., Parikh S. and Sparks D. (2010) Formation of
919 nanocrystalline todorokite from biogenic Mn oxides. *Geochim. Cosmochim. Acta* **74**,
920 3232–3245.
921 Fujii T., Moynier F., Blichert-Toft J. and Albarede F. (2014) Density functional theory
922 estimation of isotope fractionation of Fe, Ni, Cu, and Zn among species relevant to
923 geochemical and biological environments. *Geochim. Cosmochim. Acta* **140**, 553–576
924 Fujii T., Moynier F., Telouk P. and Abe M. (2010) Experimental and theoretical
925 investigation of isotope fractionation of zinc between aqua, chloro, and macrocyclic
926 complexes. *J. Phys. Chem*. **114**, 2543–2552.
927 Gou W., Li W., Ji J. and Li W. (2018) Zinc isotope fractionation during sorption onto Al
928 oxides: Atomic level understanding from EXAFS. *Environ. Sci. Technol*. **52**, 9087-
929 9096.
930 Gou W., Li W., Siebecker M., Zhu M., Li L. and Sparks D. L. (2022) Coupling molecular-
931 scale spectroscopy with stable isotope analyses to investigate the effect of Si on the
932 mechanisms of Zn-Al LDH formation on Al oxide. *Environ. Sci. Technol*. (just
933 accepted).
934 Gall, L., Williams, H. M., Siebert, C., Halliday, A. N., Herrington, R. J. and Hein, J. R.
935 (2013) Nickel isotopic compositions of ferromanganese crusts and the constancy of

deep ocean inputs and continental weathering effects over the Cenozoic. *Earth Planet. Sci. Lett.***375**, 148–155.

Ghose S. (1964) The crystal structure of hydrozincite, $Zn_5(OH)_6(CO_3)_2$. *Acta Cryst*. **17**, 1051–1057.

Grangeon, S., Fernandez-Martinez, A., Claret, F., Marty, N., Tournassat, C., Warmont, F. and Gloter, A. (2017) In situ determination of the kinetics and mechanisms of nickel adsorption by nanocrystalline vernadite. *Chem. Geol.* **459**, 24–31.

Grimme, S. (2006). Semiempirical GGA-type density functional constructed with a long-range dispersion correction. *J. Comput. Chem*. **27**, 1787-1799.

Gueguen B., Sorensen J. V., Lalonde S. V., Pena J. T., Brandy M. and Rouxel O. (2018) Variable Ni isotope fractionation between Fe-oxyhydroxides and implications for the use of Ni isotopes as geochemical tracers. *Chem. Geol.* **481**, 38–52.

Guinoiseau D., Gelabert A., Moureau J., Louvat P. and Benedetti M. F. (2016) Zn isotope fractionation during sorption onto kaolinite. *Environ. Sci. Technol*. **50**, 1844–1852.

He J., Zhang L., Jin S., Zhu Y. and Liu F. (2008) Bacterial communities inside and surrounding soil iron-manganese nodules. *Geomicrobiol. J*. **25**, 14–24.

Hein J. R., Koschinsky A., Halbach P., Manheim F. T., Bau M., Kang J. K. and Lubick N. (1997) Iron and manganese oxide mineralization in the Pacific. In *Manganese Mineralization: Geochemistry and Mineralogy of Terrestrial and Marine Deposits* (eds. K. Nicholson, J. R. Hein, B. Buhn and S. Dasgupta). Geological Society Special

956 Publication No. 119, pp. 123–138.

957 Hein, J. R., Koschinsky, A. and Kuhn, T. (2020). Deep-ocean polymetallic nodules as a
958 resource for critical materials. *Nature Reviews Earth & Environment*, **1**, 158-169.

959 Hinkle, M. A. G., Dye, K. G. and Catalano, J. G. (2017) Impact of Mn(II)-manganese oxide
960 reactions on Ni and Zn speciation. *Environ. Sci. Technol*. **51**, 3187–3196.

961 Hochella, Jr., M. F., Kasama T., Putnis A., Putnis C. V. and Moore J. N. (2005)
962 Environmentally important, poorly crystalline Fe/Mn hydrous oxides: ferrihydrite and
963 a possibly new vernadite-like mineral from the Clark Fork River Superfund Complex.
964 *Am. Mineral*. **90**, 718–724.

965 Jensen W. B. (2003) The place of zinc, cadmium, and mercury in the periodic table. *J.*
966 *Chem. Educ.* **80**, 952–961.

967 Juillot F., Marechal C., Morin G., Jouvin D., Cacaly S., Telouk P., Benedetti M. F.,
968 Ildefonse P., Sutton S., Guyot F. and Brown, G. E. (2011) Contrasting isotopic
969 signatures between anthropogenic and geogenic Zn and evidence for postdepositional
970 fractionation processes in smelter-impacted soils from Northern France. *Geochim.*
971 *Cosmochim. Acta* **75**, 2295–2308.

972 Juillot F., Marechal C., Ponthieu M., Cacaly S., Morin G., Benedetti M., Hazemann J. L.,
973 Proux O. and Guyot F. (2008) Zn isotopic fractionation caused by sorption on goethite
974 and 2-Lines ferrihydrite. *Geochim. Cosmochim. Acta* **72**, 4886–4900.

975 Keizer, M.G. and van Riemsdijk, W.H. (2009) ECOSAT: A Computer Program for the

976 Calculation of Speciation and Transport in Soil-water Systems. Wageningen
977 University, The Netherlands.
978 Komárek, M., Koretsky, C. M., Stephen, K. J., Alessi, D. S. and Chrastný, V. (2015)
979 Competitive adsorption of Cd (II), Cr (VI), and Pb (II) onto nanomaghemite: a
980 spectroscopic and modeling approach. *Environ. Sci. Technol*. **49**, 12851–12859.
981 Koschinsky A. and Hein J. R. (2003) Uptake of elements from seawater by ferromanganese
982 crusts: solid-phase associations and seawater speciation. *Mar. Geol*. **198**, 331–351.
983 Kwon K. D., Refson K. and Sposito G. (2009) Zinc surface complexes on birnessite: a
984 density functional theory study. *Geochim. Cosmochim. Acta* **73**, 1273–1284
985 Kwon K. D., Refson K. and Sposito G. (2010) Surface complexation of Pb(II) by hexagonal
986 birnessite nanoparticles. *Geochim. Cosmochim. Acta* **74**, 6731–6740.
987 Kwon K. D. and Sposito G. (2015) Mechanistic understanding of metal sorption by
988 phyllomanganates through density functional theory, Advances in the environmental
989 biogeochemistry of manganese oxides. *Am. Chem. Soc*. **51–64**.
990 Lanson B., Drits V. A., Gaillot A.-C., Silvester E., Plancon A. and Manceau A. (2002)
991 Structure of heavy-metal sorbed birnessite: Part 1. Results from X-ray diffraction. *Am.*
992 *Mineral.* **87**, 1631–1645.
993 Lanson B., Marcus M. A., Fakra S., Panfili F., Geoffroy N. and Manceau A. (2008)
994 Formation of Zn–Ca phyllomanganate nanoparticles in grass roots. *Geochim.*
995 *Cosmochim. Acta* **72**, 2478–2490.

996 Lefkowitz, J. P. and Elzinga, E. J. (2017) Structural alteration of hexagonal birnessite by
997 aqueous Mn(II): impacts on Ni(II) sorption. *Chem. Geol*. **466**, 524–532.
998 Li, Y., Zhao, X., Wu, J. and Gu, X. (2020). Surface complexation modeling of divalent
999 metal cation adsorption on birnessite. *Chem. Geol*. **551**, 119774.
1000 Little S. H., Sherman D. M., Vance D. and Hein J. R. (2014a) Molecular controls on Cu
1001 and Zn isotopic fractionation in Fe–Mn crusts. *Earth Planet. Sci. Lett.* **396**, 213–222.
1002 Little S. H., Vance D., McManus J. and Severmann S. (2016) Key role of continental
1003 margin sediments in the oceanic mass balance of Zn and Zn isotopes. *Geology* **44**,
1004 207–210.
1005 Little S. H., Vance D., Walker-Brown C. and Landing W. (2014b) The oceanic mass balance
1006 of copper and zinc isotopes, investigated by analysis of their inputs, and outputs to
1007 ferromanganese oxide sediments. *Geochim. Cosmochim. Acta* **125**, 673–693.
1008 Little, S. H., Archer, C., McManus, J., Najorka, J., Wegorzewski, A. V. and Vance, D.
1009 (2020). Toward balancing the oceanic Ni budget. *Earth Planet. Sci. Lett.* **547**, 116461.
1010 Liu, S. A., Liu, P. P., Lv, Y., Wang, Z. Z. and Dai, J. G. (2019). Cu and Zn isotope
1011 fractionation during oceanic alteration: implications for Oceanic Cu and Zn cycles.
1012 *Geochim. Cosmochim. Acta* **257**, 191-205.
1013 Manceau A., Lanson B. and Drits V. A. (2002) Structure of heavy metal sorbed birnessite:
1014 part III. The results from powder and polarized extended X-ray absorption fine
1015 structure spectroscopy. *Geochim. Cosmochim. Acta* **66**, 2639–2663.

1016 Manceau A., Lanson M. and Geoffroy N. (2007) Natural speciation of Ni, Zn, Ba and As
1017 in ferromanganese coatings on quartz using X-ray fluorescence, absorption and
1018 diffraction. *Geochim. Cosmochim. Acta* **71**, 95–128.
1019 Marcus M. A., Manceau A. and Kersten M. (2004) Mn, Fe, Zn and As speciation in a fast-
1020 growing ferromanganese marine nodule. *Geochim. Cosmochim. Acta* **68**, 3125–3136.
1021 Marechal C. N., Telouk P. and Albarede F. (1999) Precise analysis of copper and zinc
1022 isotopic compositions by plasma-source mass spectrometry. *Chem. Geol.* **156**, 251–
1023 273.
1024 Marechal C., Nicolas E., Douchet C. and Albarede F. (2000) Abundance of zinc isotopes
1025 as a marine biogeochemical tracer. *Geochem. Geophys. Geosyst.* **1**, 1015.
1026 McKenzie R. M., (1971) The synthesis of birnessite, cryptomelane, and some other oxides
1027 and hydroxides of manganese. *Mineral. Mag*. **38**, 493–503
1028 McNellis, E. R., Meyer, J. and Reuter, K. (2009). Azobenzene at coinage metal surfaces:
1029 Role of dispersive van der Waals interactions. *Phys. Rev. B*, **80**, 205414.
1030 Moon E. M. and Peacock C. L. (2012) Adsorption of Cu(II) to ferrihydrite and ferrihydrite-
1031 bacteria composites: Importance of the carboxyl group for Cu mobility in natural
1032 environments. *Geochim. Cosmochim. Acta* **92**, 203–219.
1033 Moore, C.M., et al., 2013. Processes and patterns of oceanic nutrient limitation. *Nat. Geosci*.
1034 **6**, 701–710.
1035 Nachtegaal M. and Sparks D. L. (2004) Effect of iron oxide coatings on zinc sorption

mechanisms at the clay-mineral/water interface. *J. Colloid Interface Sci.* **276**, 13–23.

Nakada, R., Tanaka, M., Tanimizu, M. and Takahashi, Y. (2017). Aqueous speciation is likely to control the stable isotopic fractionation of cerium at varying pH. *Geochim. Cosmochim. Acta* **218**, 273-290.

Nelson, J.; Wasylenki, L.; Bargar, J. R.; Brown, G. E. and Maher, K. (2017) Effects of surface disorder and surface coverage on isotopic fractionation during Zn(II) adsorption onto quartz and amorphous silica surfaces. *Geochim. Cosmochim. Acta* **215**, 354−376.

Pavlov, M., Siegbahn, P. E. and Sandström, M. (1998). Hydration of beryllium, magnesium, calcium, and zinc ions using density functional theory. *J. Phys. Chem. A* **102**, 219-228.

Peacock C. L. (2009) Physiochemical controls on the crystalchemistry of Ni in birnessite: genetic implications for ferromanganese precipitates. *Geochim. Cosmochim. Acta* **73**, 3568–3578

Peacock C. L. and Moon E. M. (2012) Oxidative scavenging of thallium by birnessite: explanation for thallium enrichment and stable isotope fractionation in marine ferromanganese precipitates. *Geochim. Cosmochim. Acta* **84**, 297–313.

Peacock C. L. and Sherman D. M. (2007a) The crystal chemistry of Ni in marine ferromanganese crusts and nodules. *Am. Mineral*. **92**, 1087–1097.

Peacock C. L. and Sherman D. M. (2007b) Sorption of Ni by birnessite: equilibrium controls on Ni in seawater. *Chem. Geol.* **238**, 94–106.

1056 Perdew J. P., Burke K. and Ernzerhof M. (1996) Generalized gradient approximation made
1057 simple. *Phys. Rev. Lett.* **77**, 3865–3868.
1058 Pfrommer B. G., Cote M., Louie S. G. and Cohen M. L. (1997) Relaxation of crystals with
1059 the quasi-Newton method. *J. Comput. Phys*. **131**, 233–240.
1060 Pokrovsky O. S., Viers J. and Freydier R. (2005) Zinc stable isotope fractionation during
1061 its adsorption on oxides and hydroxides. *J. Colloid Interface Sci.* **291**, 192–200.
1062 Post J. E. (1999) Manganese oxide minerals: crystal structures and economic and
1063 environmental significance. *Proc. Natl. Acad. Sci.* **96**, 3447–3454.
1064 Post J. E. and Appleman D. E. (1988) Chalcophanite, $ZnMn_3O_7$ $3H_2O$: New crystal-
1065 structure determinations. *Am. Mineral*. **73**, 1401–1404.
1066 Post J. E., Heaney P. J. and Hanson J. (2003) Real-time synchrotron X-ray powder
1067 diffraction studies of the structure and dehydration of todorokite. *Am. Mineral.* **88**,
1068 142–150.
1069 Pye C. C., Corbeil C. R. and Rudolph W. W. (2006) An ab initio investigation of zinc chloro
1070 complexes. *Phys. Chem. Chem. Phys.* **8**, 5428–5436.
1071 Ravel, B. Kelly, S.D., 2007. The difficult chore of measuring coordination by EXAFS. In:
1072 *X-ray Absorption Fine Structure–XAFS* **13**, pp. 150–152.
1073 Roberts D. R., Ford R. G., and Sparks D. L. (2003) Kinetics and mechanisms of Zn
1074 complexation on metal oxides using EXAFS spectroscopy. *J. Colloid Interface Sci*.
1075 **263**, 364–376.

1076 Sandstead, H.H., 2014. Zinc. In: *Handbook on the Toxicology of Metals Elsevier*, pp. 1369–
1077 1386.
1078 Schauble E. A. (2004) Applying stable isotope fractionation theory to new systems. *Rev.*
1079 *Mineral. Geochem*. **55**, 65–111.
1080 Scheinost A. C., Abend S., Pandya K. I. and Sparks D. L. (2001) Kinetic controls on Cu
1081 and Pb sorption by ferrihydrite. *Environ. Sci. Technol.* **35**, 1090–1096.
1082 Sherman D. M. and Peacock C. L. (2010) Surface complexation of Cu on birnessite (δ-
1083 MnO2): controls on Cu in the deep ocean. *Geochim. Cosmochim. Acta* **74**, 6721–6730.
1084 Simanova A. A., Kwon K. D., Bone S. E., Bargar J. R., Refson K., Sposito G. and Pena J.
1085 (2015) Probing the sorption reactivity of the edge surfaces in birnessite nanoparticles
1086 using nickel (II). *Geochim. Cosmochim. Acta* **164**, 191–204.
1087 Sinoir, M., Butler, E.C., Bowie, A.R., Mongin, M., Nesterenko, P.N., and Hassler, C.S.
1088 (2012) Zinc marine biogeochemistry in seawater: A review: *Marine & Freshwater*
1089 *Research*, v. 63, p. 644–657, doi:10.1071/MF11286
1090 Skierszkan E. K., Mayer K. U., Weis D. and Beckie R. D. (2016). Molybdenum and zinc
1091 stable isotope variation in mining waste rock drainage and waste rock at the Antamina
1092 mine, Peru. *Sci. Total Environ*. **550**, 103-113.
1093 Sorensen, J.V., Gueguen, B., Stewart, B.D., Peña, J., Rouxel, O., Toner, B.M., 2020. Large
1094 nickel isotope fractionation caused by surface complexation reactions with hexagonal
1095 birnessite. *Chem. Geol*. **537**, 119481.

1096 Spinks, S. C., and Uvarova, Y. (2019). Fractionation of Zn isotopes in terrestrial
1097 ferromanganese crusts and implications for tracing isotopically heterogeneous metal
1098 sources. *Chem. Geol*. **529**, 119-314.
1099 Sverjensky, D. A. (2005) Prediction of surface charge on oxides in salt solutions: Revisions
1100 for 1:1 (M+L-) electrolytes. *Geochim. Cosmochim. Acta* **69**, 225−257.
1101 Toner B., Manceau A., Webb S. M. and Sposito G. (2006) Zinc sorption to biogenic
1102 hexagonal-birnessite particles within a hydrated bacterial biofilm. *Geochim.*
1103 *Cosmochim. Acta* **70**, 27–43.
1104 Vance D., Little S. H., Archer C., Cameron V., Andersen M. B., Rijkenberg M. J. and Lyons
1105 T. W. (2016) The oceanic budgets of nickel and zinc isotopes: the importance of
1106 sulfidic environments as illustrated by the Black Sea. *Phil. Trans. R. Soc. A* **374**,
1107 20150294.
1108 Vanderbilt D. (1990) Soft self-consistent pseudopotentials in a generalized eigenvalue
1109 formalism. *Phys. Rev.* **B** 41, 7892–7895.
1110 Villalobos M., Bargar J. R. and Sposito G. (2005) Mechanisms of Pb(II) sorption on a
1111 biogenic manganese oxide. *Environ. Sci. Technol.* **39**, 569–576.
1112 Wang Y., Benkaddour S., Marafatto F. F. and Pena J. (2018) Diffusion- and pH-dependent
1113 reactivity of layer-type MnO2: Reactions at particle edges versus vacancy sites.
1114 *Environ. Sci. Technol*. **52**, 3476–3485.
1115 Wang Z., Kwon K. D., Peacock C., Mo X., Gou W., Feng X. and Li W. (2022) Zn stable

isotope fractionation during adsorption onto todorokite: A molecular perspective from X-ray absorption spectroscopy and density functional theory. *Geochim. Cosmochim. Acta* **327**, 116–136.

Wasylenki L. E., Rolfe B. A., Weeks C. L., Spiro T. G. and Anbar A. D. (2008) Experimental investigation of the effects of temperature and ionic strength on Mo isotope fractionation during adsorption to manganese oxides. *Geochim. Cosmochim. Acta* **72**, 5997–6005.

Wasylenki L. E., Swihart J. W. and Romaniello S. J. (2014) Cadmium isotope fractionation during adsorption to Mn oxyhydroxide at low and high ionic strength. *Geochim. Cosmochim. Acta* **140**, 212–226.

Waychunas G. A., Fuller C. C. and Davis J. A. (2002) Surface complexation and precipitate geometry for aqueous Zn(II) sorption on ferrihydrite I: X-ray absorption extended fine structure spectroscopy analysis. *Geochim. Cosmochim. Acta* **66**, 1119–1137.

Wiederhold, J. G. (2015) Metal stable isotope signatures as tracers in environmental geochemistry. *Environ. Sci. Technol.* **49**, 2606-2624.

Yan, X., Zhu, M., Li, W., Peacock, C. L., Ma, J., Wen, H., Liu, F., (2021) Cadmium isotope fractionation during adsorption and substitution with iron (oxyhydr) oxides. *Environ. Sci. Technol*. **55**, 11601–11611.

Yin H., Wang X., Qin Z., Ginder-Vogel M., Zhang S., Jiang S., Liu F., Li S., Zhang J. and Wang Y. (2018) Coordination geometry of Zn^{2+} on hexagonal turbostratic birnessites

with different Mn average oxidation states and its stability under acid dissolution. J. *Environ. Sci. (China)* **65**, 282–292.

Young E. D., Tonui E., Manning C. E., Schauble E. and Macris C. A. (2009) Spinel–olivine magnesium isotope thermometry in the mantle and implications for the Mg isotopic composition of Earth. *Earth Planet. Sci. Lett.* **288**, 524–533.

Zhao, W., Tan, W., Wang, M., Xiong, J., Liu, F., Weng, L. and Koopal, L.K. (2018) CD-MUSICEDL modeling of Pb^{2+} adsorption on birnessites: role of vacant and edge sites. *Environ. Sci. Technol*. **52**, 10522–10531.

Zhao, Y., Vance, D., Abouchami, W. and de Baar, H. J. W. (2014) Biogeochemical cycling of zinc and its isotopes in the Southern Ocean. *Geochim. Cosmochim. Acta* **125**, 653–672.

Table 1. Isotopic data of Zn in the adsorption experiments.

Experiments	Time (h)	$[Zn]_{initial}$ (mM)	Adsorbed Zn(%)	Zn/Mn (mol:mol)	pH	$\delta^{66}Zn_{aqueous}$	2SD	$\delta^{66}Zn_{adsorbed}$	2SD	$\Delta^{66}Zn_{adsorbed-aqueous}$	2SD	Mass balance
Birnessite adsorption kinetics	0.5	0.2	18.1	0.061	6	0.62	0.06	–0.61	0.03	–1.23	0.07	0.06
	1	0.2	24.8	0.084	6	0.70	0.05	–0.53	0.03	–1.22	0.06	0.07
	1.5	0.2	24.7	0.084	6	0.69	0.03	–0.48	0.05	–1.18	0.06	0.06
	3	0.2	27.7	0.094	6	0.68	0.04	–0.41	0.01	–1.09	0.04	0.05
	4	0.2	26.0	0.088	6	0.67	0.02	–0.44	0.03	–1.11	0.04	0.06
	6	0.2	28.8	0.097	6	0.65	0.03	–0.36	0.07	–1.02	0.08	0.04
	12	0.2	28.9	0.098	6	0.62	0.02	–0.28	0.03	–0.90	0.03	0.05
	24	0.2	33.6	0.114	6	0.61	0.01	–0.21	0.01	–0.81	0.04	0.03
	36	0.2	32.7	0.111	6	0.59	0.05	–0.14	0.04	–0.73	0.05	0.03
	48	0.2	32.0	0.108	6	0.59	0.04	–0.16	0.02	–0.74	0.05	0.02
	120	0.2	42.1	0.129	6	0.44	0.04	0.08	0.04	–0.36	0.06	0.01
	264	0.2	47.0	0.159	6	0.47	0.01	0.10	0.04	–0.36	0.08	0.01
	432	0.2	49.8	0.169	6	0.42	0.02	0.14	0.03	–0.30	0.05	0.01
Adsorption edges 0.2 mM	120	0.2	40.0	0.105	3	0.43	0.02	–0.06	0.01	–0.49	0.02	0.00
	120	0.2	36.1	0.122	4	0.44	0.02	0.03	0.00	–0.41	0.02	0.01
	120	0.2	50.3	0.170	5	0.49	0.02	0.06	0.03	–0.43	0.03	–0.01
	120	0.2	55.4	0.187	6	0.47	0.03	0.22	0.04	–0.25	0.05	0.05
	120	0.2	75.6	0.256	7	0.34	0.03	0.24	0.01	–0.10	0.04	–0.01
	120	0.2	93.7	0.317	8	0.35	0.01	0.29	0.04	–0.06	0.04	0.00
Adsorption isotherms pH 3	120	0.05	43.9	0.037	3	0.46	0.00	0.05	0.04	–0.41	0.04	0.01
	120	0.07	34.9	0.041	3	0.43	0.03	–0.02	0.04	–0.45	0.05	–0.01
	120	0.1	45.4	0.077	3	0.54	0.02	0.00	0.05	–0.54	0.05	0.01
	120	0.2	40.1	0.105	3	0.43	0.02	–0.06	0.01	–0.49	0.02	0.00
	120	0.3	23.7	0.121	3	0.37	0.02	–0.13	0.02	–0.50	0.03	–0.03

Note. $^{66}Zn_{stock}$ was 0.28 ± 0.06‰ (2SD, n = 6). Each isotopic data was the average value calculated from three measurements. The 2 SD

values were the internal precisions of replicates. Mass balance offset = ($\delta^{66}Zn_{aqueous}$ (1-adsorbed %) +$\delta^{66}Zn_{adsorbed}$ adsorbed %)- $\delta^{66}Zn_{stock}$.

Table 2. Fitting results of the EXAFS spectra for Zn-birnessite samples and model compounds ($S_0^2 = 0.97$)

Samples	Shell no.	Path	CN	R (Å)	σ^2(Å^2)	R-factor	ΔE_0 (eV)
Zinc hydroxide	1	Zn–O	3.7	1.98	0.006	0.0009	5.16
	2	Zn–Zn	10.4	3.23	0.009		
	3	Zn–Zn	3.8	4.62	0.004		
Hydrozincite	1	Zn–O	4.5	1.98	0.009	0.0082	–5.98
	2	Zn–Zn	1.4	3.12	0.012		
	2	Zn–Zn	2.2	3.52	0.006		
Zn tetrahedra	1	Zn–O	3.3	1.97			
	2	Zn–Mn	2.9	3.35			
	2	Zn–Mn	2.0	3.50			
Chalcophanite	1	Zn–O	3	2.07			
	1	Zn–O	3	2.14			
	2	Zn–Mn	3	3.49			
	2	Zn–Mn	3	3.50			
pH 8_0.2 mM	1	Zn–O	2.1	2.01	0.005	0.0007	7.24
	1	Zn–O	2.3	2.17	0.015		
	2	Zn–Mn	3.5	3.49	0.015		
pH 6_0.2 mM	1	Zn–O	2.9	2.04	0.008	0.0005	5.86
	1	Zn–O	2.7	2.18	0.020		
	2	Zn–Mn	7.1	3.49	0.016		
pH 3_0.2 mM	1	Zn–O	2.5	2.03	0.006	0.0008	5.97
	1	Zn–O	2.5	2.15	0.012		
	2	Zn–Mn	6.3	3.50	0.011		
pH 3_0.1 mM	1	Zn–O	3.0	2.04	0.004	0.0041	3.02
	1	Zn–O	3.0	2.17	0.010		
	2	Zn–Mn	7.5	3.52	0.012		
pH 3_0.05 mM	1	Zn–O	2.6	2.03	0.001	0.0011	5.72
	1	Zn–O	2.6	2.18	0.003		
	2	Zn–Mn	7.7	3.52	0.012		

The parameters of Zn tetrahedra are from EXAFS fits for Zn adsorbed birnessite mainly in tetrahedral coordination (sample ZnBi8) (Manceau et al., 2002). Chalcophanite values are from XRD (Post and Appleman, 1988). Bir pH 3_0.2 means Zn local structure on birnessite at pH 3 and initial Zn concentration of 0.2 mM.

Table 3. DFT-calculated structure parameters of Zn surface complexes formed in the birnessite nanodisk model

	TCS		DCS			DES	
	$Zn{\cdot}3H_2O$	$Zn{\cdot}1H_2O$	$Zn{\cdot}4H_2O$	$Zn{\cdot}4H_2O$[a]	$Zn{\cdot}2H_2O$	$Zn{\cdot}3H_2O$[c]	$Zn{\cdot}3H_2O$[d]
$d(Zn–O_{1st})$	2.07	1.91	1.95	1.93	1.85	2.01	2.07
	2.09	1.95	1.96	1.95	1.90	2.08	2.09
	2.08	1.95	1.98	1.98	2.14	2.13	2.10
	2.18	2.09	2.03	2.03	2.10	2.20	2.11
	2.17					2.20	2.23
	2.17					2.25	2.26
	<2.13>	<1.98>	<1.98>	<1.97>	<2.00>	<2.15>	<2.16>
C.N.	6	4	4[b]	4[b]	4	6	6
$d(Zn–Mn_{1st})$	3.50	3.29	3.27	3.32	3.25	2.96	2.97
	3.51	3.31	3.36	3.36	3.16	2.98	3.13
	3.50	3.33					
	3.50	3.32					
	3.51	3.32					
	3.50	3.31					
	<3.50>	<3.31>	<3.32>	<3.34>	<3.21>	<2.97>	<3.05>
C.N.	6	6	2	2	2	2	2

[a] Calculation with dispersion correction (DFT–D).

[b] Initial octahedral arrangement always ended up with tetrahedral coordination.

[c] Complex coordinated with terminal bridging oxygen.

[d] Complex coordinated with bridging oxygen.

1186 **Table 4**. Model parameters for protons and Zn adsorption to birnessite.

Protons complex on external surface	Δz_0	Δz_1	Δz_2	log *K*
$\equiv MnOH^{-1/3} + H^+ = \equiv MnOH_2^{+2/3}$	1	0	0	4.6[a]
$\equiv MnOH^{-1/3} + Na^+ = \equiv MnOH^{-1/3}\ldots Na^+$	0	1	0	–0.6[a]
$\equiv MnOH^{-1/3} + H^+ + NO_3^- = \equiv MnOH_2^{+2/3}\ldots NO_3^-$	0	–1	0	3.92[a]
Protons complex on internal surface	Δz_0			log *K*
$\equiv Mn_2O^{-2/3} + H^+ = \equiv Mn_2OH^{+1/3}$	1			1.2[a]
Zn complex on external surface	Δz_0	Δz_1	Δz_2	log *K*
$2 \equiv MnOH^{-1/3} + Zn^{2+} + H_2O = (\equiv MnOH)_2ZnOH^{+1/3} + H^+$	0.51	0.49	0	–3.54
Zn complex on internal surface	Δz_0			log *K*
$3 \equiv Mn_2O^{-2/3} + Zn^{2+} = (\equiv Mn_2O)_3Zn^0$	2			–0.36

External surface: SSA[b] = 176 $m^2\ g^{-1}$; site density[c] = 14.9 sites nm^{-2}; $C_1 = C_2 = 2.5$ F m^{-2}.
Interlayer surface: SSA[b] = 729 $m^2\ g^{-1}$; site density[c] = 8.34 sites nm^{-2}; C = 2.0 F m^{-2}.
[a] From Li et al. (2020). [b] The SSA of external and internal surfaces are assumed based on the calculation of the crystal structure of birnessite (Zhao et al., 2018). [c] The site densities of birnessite are calculated according to Mn AOS and the crystal structure based on Zhao et al. (2018).

1187
1188
1189
1190